A hybrid spectral/finite-difference large-eddy simulator of turbulent processes in the upper ocean

Andrés E. Tejada-Martínez [a,*], Chester E. Grosch [b], Ann E. Gargett [b], Jeff A. Polton [c], Jerome A. Smith [d], J.A. MacKinnon [d]

[a] Department of Civil and Environmental Engineering, University of South Florida, Tampa, FL, United States
[b] Ocean, Earth and Atmospheric Sciences and Center for Coastal Physical Oceanography, Old Dominion University, Norfolk, VA, United States
[c] Proudman Oceanographic Laboratory, Liverpool, United Kingdom
[d] Scripps Institution of Oceanography, University of California, San Diego, La Jolla, CA, United States

ARTICLE INFO

ABSTRACT

A three-dimensional numerical model for large-eddy simulation (LES) of oceanic turbulent processes is described. The numerical formulation comprises a spectral discretization in the horizontal directions and a high-order compact finite-difference discretization in the vertical direction. Time-stepping is accomplished via a second-order accurate fractional-step scheme. LES subgrid-scale (SGS) closure is given by a traditional Smagorinsky eddy-viscosity parametrization for which the model coefficient is derived following similarity theory in the near-surface region. Alternatively, LES closure is given by the dynamic Smagorinsky parametrization for which the model coefficient is computed dynamically as a function of the flow. Validation studies are presented demonstrating the temporal and spatial accuracy of the formulation for laminar flows with analytical solutions. Further validation studies are described involving direct numerical simulation (DNS) and LES of turbulent channel flow and LES of decaying iso-tropic turbulence. Sample flow problems include surface Ekman layers and wind-driven shallow water flows both with and without Langmuir circulation (LC), generated by wave effects parameterized via the well-known Craik–Leibovich (C–L) vortex force. In the case of the surface Ekman layers, the inner layer (where viscous effects are important) is not resolved and instead is parameterized with the Smago-rinsky models previously described. The validity of the dynamic Smagorinsky model (DSM) for parame-terizing the surface inner layer is assessed and a modification to the surface stress boundary condition based on log-layer behavior is introduced improving the performance of the DSM. Furthermore, in Ekman layers with wave effects, the implicit LES grid filter leads to LC subgrid-scales requiring ad hoc modeling via an explicit spatial filtering of the C–L force in place of a suitable SGS parameterization.

© 2009 Elsevier Ltd. All rights reserved.

1. Introduction

A parallel, hybrid spectral/finite-difference solver of the incompressible Navier–Stokes equations under the Boussinesq approximation is developed with the goal of performing large-eddy simulations (LES) of turbulent processes in the ocean. The solver uses a second-order time-accurate fractional-step method; horizontal directions are discretized spectrally using Fourier transforms and the vertical direction is discretized using high-order (fifth and sixth-order) compact finite-difference schemes. Finite differences allow for grid stretching in the vertical in order to resolve expected strong vertical gradients in scalars and velocity. The solver is equipped with subgrid-scale stress parameterizations

suitable for LES. Boundary conditions can be assigned as prescribed velocity components or as prescribed shear stresses at the bottom and top bounding surfaces perpendicular to the vertical direction. In the case of a deep bottom, the solver uses a sponge layer in the lower region of the domain in order to absorb incoming internal waves due to stratification. Parallelization is achieved via message passing interface (MPI) protocol using the same structure described by Winters et al. (2004).

The fractional-step algorithm consists of the pressure correction method on a non-staggered grid of Armfield and Street (2000). Such a scheme is attractive because it avoids the complexities of traditional schemes on non-staggered grids while achieving second-order accuracy for momentum and continuity. More specifically, the non-staggered grid avoids interpolations from grid points to cell centers and vice versa. Fractional-step algorithms require solution of the momentum equation leading to an intermediate non-solenoidal velocity followed by a Poisson's equation for pressure leading to a velocity correction enforcing continuity.

* Corresponding author. Address: Department of Civil and Environmental Engineering, College of Engineering, University of South Florida, 4202 East Fowler Avenue, Tampa, FL 33620, United States.
E-mail address: aetejada@eng.usf.edu (A.E. Tejada-Martínez).

In the method of Armfield and Street (2000), nonlinear terms in the momentum-solve are discretized explicitly with the second-order Adams–Bashforth scheme while linear viscous terms are discretized implicitly with the second-order Crank–Nicholson scheme. This second-order accurate time discretization of the momentum equation is complemented with a second-order accurate time discretization of the continuity equation inherently satisfied through a Poisson's equation for pressure, as shown by Fringer et al. (2003).

A similar solver to the present model is that of Slinn and Riley (1998). Both models use a similar time-stepping algorithm and both use a single spatial (collocated) grid for all variables. Furthermore, both models are hybrid, employing Fourier transforms in two directions and compact finite differences in the third direction. Three major differences between the two models are (1) the use of higher order compact finite-difference schemes in the present model, (2) the implicit treatment of the molecular viscous stress in the present model and (3) inclusion of the gradient of pressure in the momentum equation in the present model. The model of Slinn and Riley (1998) uses fourth-order compact finite differences in the vertical direction. Meanwhile, the present model uses fifth- and sixth-order compact finite differences in the vertical direction. The current model treats the molecular viscous stress implicitly via the Crank–Nicholson scheme whereas the model of Slinn and Riley treats it explicitly via Adams–Bashforth. Explicit treatment of the molecular viscous stress terms leads to more stringent restrictions of the time step. Inclusion of the pressure gradient in our momentum equation (following the work of Armfield and Street (2000)) leads to a second-order accurate in time fractional-step scheme. The model of Slinn and Riley excludes this pressure gradient reducing the accuracy of their scheme to first-order in time.

In this article, the previously described discretization is shown to yield expected rates of spatial and temporal convergence. Furthermore, the above-mentioned discretization is validated by performing LES of benchmarks problems such as turbulent channel flow and isotropic turbulence. The discretization is also shown to be effective for oceanic turbulent processes in shallow water and within the surface mixed layer in deep water.

The wide range of spatial and temporal scales in typical turbulent processes makes their explicit computation untractable. Computational constraints make it impossible to resolve the inner layer in typical oceanic turbulent boundary layers occurring at extremely high-Reynolds number. Following Piomelli and Balaras (2002), boundary layers can be divided into two regions: the inner layer where viscous effects are important and the outer layer where direct viscous effects on mean velocity are negligible. Two alternatives exist for dealing with the difficulty in resolving the inner layer. In one alternative, the turbulence is simulated at a much lower Reynolds number than in the ocean. The relatively low-Reynolds number of the simulated flow permits near full resolution of boundary layers through either direct numerical simulation (DNS) or LES with near-wall partial resolution (LES-NWR), the latter term coined by Pope (2000). Although LES-NWR directly refers to partially resolved wall-bounded boundary layers, this terminology applies to the resolution of boundary layers in general.

In DNS all of the scales in the turbulence are explicitly computed or resolved, while in LES the more energetic scales are resolved and the remaining smaller scales are parameterized. Furthermore, in principle, the LES should have sufficient resolution to capture a part of the inertial sub-range. The importance of this is that scales within and below the inertial sub-range are universal and thus can be parameterized with a subgrid-scale model applicable to any flow condition. Scales within and below the inertial sub-range become smaller as bottom or surface boundary layers are approached, requiring smaller grid sizes near those regions, ultimately leading to LES-NWR.

A drawback of LES-NWR is its limitation to low-Reynolds number flows, much lower than those typically observed in the actual ocean. In this case, the simulated flow may be strongly affected by low-Reynolds number effects and may not scale-up favorably to the actual flow at a greater Reynolds number. Thus, comparison of computational results with observational field data is crucial.

An alternative to LES-NWR is to perform LES with near-wall modeling or LES-NWM (Pope, 2000). In this approach, small turbulent scales and the inner layer are not resolved and instead are parameterized. In LES-NWM, parameterizations typically consist of those used for LES-NWR modified to capture the net effect of the unresolved inner layer in a Reynolds-average sense (Piomelli and Balaras, 2002; Sullivan et al., 1994). A drawback of this approach is that results near the unresolved inner layer tend to heavily depend on the parameterization. A extensive review of LES-NWM is given by Piomelli and Balaras (2002). Here we limit our discussion of LES-NWM to issues related to our computations.

In LES, the governing equations are spatially filtered leading to a subfilter-scale (SFS) stress (often referred to as the subgrid-scale (SGS) stress) which must be parameterized. This stress accounts for the effect of the unresolved small scales on the resolved larger scales. Reference to SGS instead of SFS is appropriate for implicit LES methodologies where a combination of the grid and numerical scheme assumes the role of the filter, often referred to as the grid filter. In well-resolved regions, the SGS scales are within the inertial sub-range, and the resolved scales (given by the LES solution) tend to be insensitive to details of the SGS stress parametrization. However, in poorly resolved or unresolved regions, such as inner layers in LES-NWM, the resolved scales greatly depend on the SGS stress parametrization. In these cases, the unresolved fraction of the total turbulence increases as the unresolved inner layer is approached. Thus, often inner layer parameterizations in LES-NWM resemble those in RANS-based models. For example, in the LES-NWM of tidal boundary layers of Li et al. (2005), the SGS stress at the bottom is given through a quadratic drag law based on log-layer similarity theory. The same formulation is used to set the bottom SGS stress in the RANS-based coastal circulation computations of Durski et al. (2004). Other LES-NWM involving similar inner layer parameterizations within the geophysical flows community include the atmospheric boundary layer simulations of Beare et al. (2006) and the oceanic surface layer simulations of McWilliams et al. (1997), Skyllingstad and Denbo (1995) and Zikanov et al. (2003). Note that in these simulations, molecular viscosity is deemed much smaller than the turbulent viscosity thus the viscous stress is neglected with respect to the SGS stress. Furthermore, given that the inner layer is not resolved, the SGS stress is designed so that it matches the prescribed surface stress thereby transmitting fluxes from the surface to the interior in the absence of the viscous stress. This in contrast to the LES-NWR approach in which the viscous stress matches the surface stress while the SGS stress decreases to zero as the surface is approached.

Since its derivation in the early 1990s, the dynamic Smagorinsky SGS stress model (Germano et al., 1991; Lilly, 1992) has gained popularity due to its dynamically computed model coefficient based on local flow conditions allowing it to adapt to numerous conditions. The derivation of the dynamic Smagorinsky model (DSM) assumes that the computation resolves down to within the inertial sub-range, relying on the scale-similarity characterizing this region. Thus, traditionally, the model has been used in LES-NWR. Recently, the DSM has also been used for LES-NWM of the atmospheric boundary layer (Porté-Agel et al., 2000). In these simulations, the DSM has been shown to yield low values of the SGS stress in the surface region which has been attributed to a lack of resolution of the inertial sub-range in that region, clearly the case since the inner layer is not resolved. In order to alleviate this problem, Lund et al. (2003), following ideas proposed by Sullivan

et al. (1994), introduced a hybrid SGS parametrization smoothly varying between the DSM far from the surface and a more traditional eddy-viscosity parametrization based on Reynolds-averaged near-surface similarity close to the surface. Porté-Agel et al. (2000) introduced a new dynamic Smagorinsky parametrization for which near-surface resolution of the inertial sub-range is not required, ultimately leading to a scale-dependent parameterization. Similar to the parametrization of Lund et al. (2003), their parametrization also led to higher values of the SGS stress.

Use of the DSM for LES-NWM of the ocean surface mixed layer has been limited to the simulations of Zikanov et al. (2003). They did not report the difficulties described earlier for the case of LES-NWM of the atmospheric boundary layer. Here we demonstrate that for LES-NWM of the ocean surface mixed layer, the DSM does lead to excessive low values of the SGS stress near the surface. For staggered grid methods, such as the method used by Zikanov et al. (2003), the surface wind stress boundary condition is not imposed at the surface, but rather at a distance half the vertical grid cell size away from the surface. Such a condition greatly alleviates the difficulties of the DSM near the surface, as will be shown through our non-staggered grid method.

In the upcoming sections, the dimensionless governing equations are described along with appropriate parameterizations of the SGS stress. This will be followed by a description of the fractional-step scheme and the spatial discretization. Applications of the solver to oceanic turbulence in shallow and deep water involving LES-NWR and LES-NWM will be shown. We will focus on a simple modification to the surface SGS stress boundary condition leading to an improvement in the performance of the DSM for LES-NWM on non-staggered grids. The resulting boundary condition enforces an SGS stress behavior consistent with log-layer similarity. We will also show results from LES of Langmuir circulation (LC) in shallow water and in deep water. LC consists of parallel, counter-rotating vortices approximately aligned in the direction of the wind. In our formulation, LC is generated by the Craik–Leibovich (C–L) vortex force (Craik and Leibovich, 1976) in the momentum equation parameterizing the interaction between surface waves and the wind-driven shear current. Note that this interaction and thus the C–L force mechanism do not involve viscous processes, thus the C–L force can be used to represent LC regardless of whether or not LES-NWR or LES-NWM is being performed. We will highlight the need to spatially filter the C–L vortex force in order to damp unbounded energy growth injected by the force through subgrid-scale LC. This low-pass spatial filtering operation acts as a surrogate model of LC subgrid-scales induced by the LES grid filter.

Validation studies demonstrating the temporal and spatial convergence of the discretization will be presented in Appendix. Finally, results from application of the discretization to canonical turbulence problems (such as turbulent channel flow and decaying isotropic turbulence) will be shown.

2. Governing equations

2.1. The filtered equations

The Boussinesq approximated filtered Navier–Stokes equations augmented with the Craik–Leibovich vortex force accounting for the phased-averaged surface waves and their generation of LC are

$$\frac{\partial \bar{u}_i}{\partial x_i} = 0,$$

$$\frac{\partial \bar{u}_i}{\partial t} + \bar{u}_j \frac{\partial \bar{u}_i}{\partial x_j} + \frac{1}{Ro} F_i = -\frac{\partial \overline{\Pi}}{\partial x_i} + Ri(\bar{\theta} - \theta_b)\delta_{i3} + \frac{1}{Re}\frac{\partial^2 \bar{u}_i}{\partial x_j^2} + \frac{\partial \tau_{ij}^{sgs}}{\partial x_j} + \frac{1}{La_t^2}\epsilon_{ijk}\phi_j^s \bar{\omega}_k,$$

$$\frac{\partial \bar{\theta}}{\partial t} + \left(\bar{u}_j + \frac{1}{La_t^2}\phi_j\right)\frac{\partial \bar{\theta}}{\partial x_j} = \frac{1}{RePr}\frac{\partial^2 \bar{\theta}}{\partial x_j^2} + \frac{\partial \lambda_j^{sgs}}{\partial x_j}, \qquad (1)$$

where ϵ_{ijk} is the totally antisymmetric third rank tensor and (x_1, x_2, x_3) is a right-handed coordinate system with x_1 and x_2 denoting the horizontal directions and x_3 denoting the vertical direction. The filtered velocity vector is $(\bar{u}_1, \bar{u}_2, \bar{u}_3)$ and $\bar{p}$ is the filtered pressure divided by the reference density, ρ_o. The over-bar denotes the application of a spatial filter. The filtered temperature is $\bar{\theta}$ and $\theta_b = \langle \bar{\theta}\rangle_h$ is the bulk temperature with $\langle \cdot \rangle_h$ denoting an average over horizontal directions x_1 and x_2. Note that the temperature has been decomposed as

$$\bar{\theta} = \theta_b + \bar{\theta}', \qquad (2)$$

and thus the filtered pressure in (1) is the pressure that remains after the component of pressure that is in hydrostatic balance with the bulk temperature field is removed. This treatment of the buoyancy term in the momentum equation has been previously used by others (e.g. Armenio and Sarkar, 2002; Basu and Porté-Agel, 2006).

Equations in (1) have been made dimensionless with half-depth, δ, and wind stress friction velocity, u_τ. The Reynolds number is $Re = u_\tau \delta / v$ and the Prandtl number is $Pr = v/\kappa$ where v is the molecular kinematic viscosity and κ is the molecular diffusivity. The subgrid-scale stress, τ_{ij}^{sgs}, is defined as

$$\tau_{ij}^{res} \equiv \bar{u}_i \bar{u}_j - \overline{u_i u_j}, \qquad (3)$$

and the subgrid-scale buoyancy flux is defined as

$$\lambda_j^{sgs} = \bar{u}_j \bar{\theta} - \overline{u_j \theta}. \qquad (4)$$

The last term on the right-hand side of the momentum equation in (1) is the C–L vortex force defined as the Stokes drift velocity crossed with the filtered vorticity $\bar{\omega}_i$ (Craik and Leibovich, 1976). The C–L vortex force is a parameterization of the interaction between phase-averaged surface waves and the wind-driven current leading to Langmuir turbulence characterized by LC. The non-dimensional Stokes drift velocity is defined as

$$\phi_1^s = \frac{\cosh(2\kappa x_3)}{2\sinh^2(\kappa H)} \quad \text{and} \quad \phi_2^s = \phi_3^s = 0, \qquad (5)$$

where $H = 2\delta$ is the depth of the domain and κ is the dominant wavenumber of the phased-averaged surface gravity waves.

The Stokes-modified Coriolis force, F_i, in (1) is $(-\bar{u}_2 - \phi_2^s/La_t^2, \bar{u}_1 + \phi_1^s/La_t^2, 0)$ and the Rossby number is $Ro = u_*/f\delta$ with f the Coriolis parameter. Meanwhile, the turbulent Langmuir number appearing in the Coriolis force and C–L vortex force is defined as $La_t = (u_\tau/u_s)^{1/2}$, where $u_s = \omega \kappa a^2$ is a characteristic Stokes drift velocity with ω being the dominant frequency; κ, the dominant wavenumber and a, the amplitude of the surface waves.

The non-dimensional, modified, filtered pressure is defined as

$$\overline{\Pi} = \bar{p} + \frac{1}{2}\Gamma, \qquad (6)$$

where $\bar{p}$ is the filtered dynamic pressure divided by density, ρ_o, and

$$\Gamma = \frac{1}{La_t^4}\phi_i^s \phi_i^s + \frac{2}{La_t^2}\bar{u}_i \phi_i^s. \qquad (7)$$

The buoyancy term in the momentum equation involves the Richardson number defined as

$$Ri = \frac{\eta g \delta^2}{u_\tau^2}\left(\frac{d\bar{\theta}}{dx_3}\right)_{x_3 = 0}, \qquad (8)$$

where $(d\bar{\theta}/dx_3)_{x_3=0}$ is the fixed vertical temperature gradient at the thermocline (i.e. at the bottom of the domain) in our stratified surface mixed layer flows, and η is the coefficient of thermal expansion.

2.2. Subgrid-scale closure

The SGS stress, τ_{ij}^{sgs}, is parameterized using the Smagorinsky closure (Smagorinsky, 1963) via a dynamic procedure discussed by

Lilly (1992) and references within. Specifically, the deviatoric part of τ_{ij}^{sgs} (i.e. $\tau_{ij}^{sgsd} \equiv \tau_{ij}^{sgs} - \delta_{ij}\tau_{kk}^{sgs}/3$) is parameterized using the dynamic Smagorinsky closure and the dilatational part (i.e. $\delta_{ij}\tau_{kk}^{sgs}/3$) is added to the pressure. The Smagorinsky closure expresses the deviatoric part of the SGS stress as

$$\tau_{ij}^{sgsd} = 2 \underbrace{(C_s\overline{\varDelta})^2|\overline{S}|}_{\text{eddy viscosity, } v_e} \overline{S}_{ij}, \qquad (9)$$

where $\overline{\varDelta}$ is the width of the grid filter (i.e. the smallest characteristic length scale resolved by the discretization), C_s is the Smagorinsky coefficient, $\overline{S}_{ij} = (\bar{u}_{i,j} + \bar{u}_{j,i})/2$ is the filtered strain rate tensor and $|\overline{S}| = (2\overline{S}_{ij}\overline{S}_{ij})^{1/2}$ is its norm. Note that the splitting of τ_{ij}^{sgs} into a deviatoric part, τ_{ij}^{sgsd}, and a dilatational part is done for mathematical consistency, as both sides of (9) are trace free. The model coefficient is computed dynamically (Lilly, 1992) based on resolved fields as

$$(C_s\overline{\varDelta})^2 = \frac{1}{2}\frac{\langle L_{ij}M_{ij}\rangle}{\langle M_{kl}M_{kl}\rangle}, \qquad (10)$$

where

$$L_{ij} = \widetilde{\bar{u}_i\bar{u}_j} - \widetilde{\bar{u}}_i\widetilde{\bar{u}}_j, \qquad (11)$$

and

$$M_{ij} = |\widetilde{\overline{S}|\overline{S}}_{ij} - \beta^2|\widetilde{\overline{S}}|\widetilde{\overline{S}}_{ij}. \qquad (12)$$

An over-tilde, $\tilde{\cdot}$, denotes the application of a homogeneous, low-pass, spatial test filter in the x_1 and x_2 directions. Angle brackets in (10) denote averaging over homogeneous directions as means of preventing instabilities due to potential negative values of the model coefficient. Finally, β is a parameter referred to as the filter width ratio, often approximated as the test filter width divided by the grid cell size, h. Simulations with the dynamic Smagorinsky model to be presented later were performed using the well-known box filter of width $2h$ (Pope, 2000) approximated using the trapezoidal rule. The width of the resulting discrete filter is $\sqrt{6}h$ (Lund, 1997), thus $\beta = \sqrt{6}$.

The derivation of the model coefficient in (10) is based on the Germano identity (Germano et al., 1991) which relates SGS stresses at two different scales ultimately leading to a model coefficient (i.e. the Smagorinsky coefficient) determined dynamically as a function of resolved quantities. The grid-level SGS stress arises from filtering at the grid-scale (defined by the grid filter) while the test-level SGS stress arises from filtering at a test-scale (defined by a test filter) usually taken as twice the grid-scale. Assuming scale-invariance, both SGS stresses are modeled via Smagorinsky models with identical Smagorinsky coefficients. This assumption is valid if the grid-scale and test-scale are within the inertial sub-range of the turbulence. However, often the grid-scale and/or test-scale fall outside of the inertial sub-range as is the case when inner layers are not resolved.

Similarly, the subgrid-scale buoyancy flux is parameterized as

$$\lambda_j^{sgs} = \underbrace{(C_{\bar{\theta}}\overline{\varDelta})^2|\overline{S}|}_{\text{eddy diffusivity, } \kappa_e} \frac{\partial\bar{\theta}}{\partial x_j}, \qquad (13)$$

where the model coefficient is computed as

$$(C_{\bar{\theta}}\overline{\varDelta})^2 = \frac{1}{2}\frac{\langle \mathscr{L}_i\mathscr{M}_i\rangle}{\langle \mathscr{M}_k\mathscr{M}_k\rangle}, \qquad (14)$$

with

$$\mathscr{L}_i = \widetilde{\bar{\theta}\bar{u}_j} - \widetilde{\bar{\theta}}\widetilde{\bar{u}}_j, \qquad (15)$$

and

$$\mathscr{M}_i = |\widetilde{\overline{S}|\frac{\partial\bar{\theta}}{\partial x_i}} - \beta^2|\widetilde{\overline{S}}|\frac{\partial\widetilde{\bar{\theta}}}{\partial x_i}. \qquad (16)$$

Applications of the dynamic Smagorinsky model in LES-NWM of geophysical flows are recent and have been primarily performed for the atmospheric boundary layer (see Porté-Agel et al., 2000). For the most part, LES-NWM of geophysical flows have been conducted using the Smagorinsky model without dynamic determination of the model coefficient. Instead, the model coefficient or better yet the mixing length, $\lambda \equiv C_s\overline{\varDelta}$, is obtained by following similarity theory which ultimately leads to a representation satisfying the condition that $\lambda \sim z$ (Mason and Thomson, 1992) where z is the distance to the bottom, say in an atmospheric boundary layer. The same behavior of the model coefficient has been adopted by Lewis (2005) in his LES-NWM of the near-surface region of the upper ocean mixed layer (UOML). We have adopted the same behavior in our simulations of the UOML to be presented later. In this case, the model coefficient is obtained from

$$\frac{1}{(C_s\overline{\varDelta})^2} = \frac{1}{(C_o\overline{\varDelta})^2} + \frac{1}{\kappa^2(z+z_o)^2}. \qquad (17)$$

Furthermore, following Lewis (2005) and references within, we take $\kappa_e = v_e/Pr$ in (13). In Eq. (17), z is the dimensionless distance to the top surface and z_o is the sea surface roughness length scale both non-dimensionalized with δ, $\kappa = 0.4$ is the von Kármán constant, $C_o\overline{\varDelta}$ is the mixing length far from the surface and C_o is an adjustable parameter usually ranging from 0.1 to 0.3. In our implementation we have taken $C_o = 0.16$. Furthermore, we have taken $\overline{\varDelta} = (\Delta x_1\Delta x_2\Delta x_3)^{1/3}$. Note that Δx_3 varies with depth. Roughness length scale z_o has been taken as O(0.1 m) following Lewis (2005), who used the UK Meteorological Office LES code (Blasius version 3.03) and McWilliams et al. (1997), who used the subgrid-scale model of Sullivan et al. (1994). Non-dimensionalizing with a half-depth of 45 m, which the half-depth of the mixed layers in the simulations of Lewis (2005) and McWilliams et al. (1997), leads to a dimensionless roughness length of O(0.00222). In the absence of a better approximation, we have chosen the dimensionless roughness length as the dimensionless distance between the domain surface and the first horizontal plane of grid points below the surface, which is O(0.001) for the simulations to be presented later. Coefficient C_o is taken as 0.16, following the analytical work of Lilly as described by Pope (2000). This result is valid for high-Reynolds number turbulence under the assumption that resolved scales are within the inertial sub-range, which is indeed the case in LES-NWM far from boundaries. Note that near the surface, the C_o term in Eq. (17) (i.e. the first term on the right-hand side (rhs) of (17)) is negligible compared to the second term in the rhs of (17). The second term decreases with depth and thus $C_s \approx C_o = 0.16$ in regions far below the surface.

3. Numerical method

3.1. Temporal discretization

The non-dimensionalized governing equations in (1) with appropriate boundary conditions are solved on a non-staggered grid using the second-order time-accurate semi-implicit fractional-step method analyzed by Armfield and Street (2000). Fractional-step methods integrate the governing equations in a segregated manner. In other words, the momentum equations are first solved for the velocity and then some form of Poisson's equation is solved for pressure. Poisson's equation is derived using the continuity and momentum equations. Thus, the solution of this equation provides the pressure and also acts to enforce continuity.

Our experience with the fractional-step method previously mentioned has been similar to that of Armfield and Street (2000) in that spurious oscillations of the pressure, characteristic of non-staggered grids, are inherently suppressed by the method. Armfield and Street implemented their fractional-step method

using a low-order, finite volume spatial discretization and did not observe spurious pressure oscillations. In our implementation, a high-order, spectral/finite-difference spatial discretization also helps to minimize the spurious pressure oscillations, as noted by Shih et al. (1989) and Lamballais et al. (1998).

For simplicity, advection, the Coriolis force, the gradient of the SGS stress and the C–L vortex force are gathered into function H_i as

$$H_i(\bar{u}_k) = \bar{u}_j \frac{\partial \bar{u}_i}{\partial x_j} + \frac{F_i}{Ro} - Ri(\bar{\theta} - \theta_b)\delta_{i3} - \frac{\partial \tau_{ij}^{sgsd}}{\partial x_j} - \epsilon_{ij3}\frac{1}{Ro}\left(\bar{u}_j + \frac{1}{La_t^2}\phi_j^s\right) - \epsilon_{ijk}\frac{1}{La_t}\phi_j^s\bar{\omega}_k.$$
(18)

Reverting to vector notation (i.e. $\bar{\boldsymbol{u}} = (\bar{u}_1, \bar{u}_2, \bar{u}_3)$, $\boldsymbol{\nabla} = (\partial_{x_1}, \partial_{x_2}, \partial_{x_3})$, $\boldsymbol{H} = (H_1, H_2, H_3)$ and so on) the terms in (18) are explicitly discretized using the second-order time-accurate Adams–Bashforth scheme as

$$\boldsymbol{N}(\bar{\boldsymbol{u}}^n, \bar{\boldsymbol{u}}^{n-1}) = \frac{3}{2}\boldsymbol{H}(\bar{\boldsymbol{u}}^n) - \frac{1}{2}\boldsymbol{H}(\bar{\boldsymbol{u}}^{n-1}),$$
(19)

where the superscripts refer to time steps n and $n-1$. Using the second-order time-accurate Crank–Nicholson scheme to discretize the molecular viscous stress, the semi-discrete momentum equation may be expressed as

$$\left(\frac{1}{\Delta t} - \frac{1}{2Re}\boldsymbol{\nabla}^2\right)\Delta \bar{\boldsymbol{u}}_*^{n+1} = -\boldsymbol{N}(\bar{\boldsymbol{u}}^n, \bar{\boldsymbol{u}}^{n-1}) + \frac{1}{Re}\boldsymbol{\nabla}^2 \bar{\boldsymbol{u}}^n - \boldsymbol{\nabla}\bar{p}^n \quad \text{in } \Omega,$$
$$\bar{\boldsymbol{u}}_*^{n+1} = \bar{\boldsymbol{u}}^n + \Delta \bar{\boldsymbol{u}}_*^{n+1} \quad \text{in } \Omega + \partial\Omega,$$
(20)

where $\bar{\boldsymbol{u}}_*^{n+1} = (\bar{u}_{1*}^{n+1}, \bar{u}_{2*}^{n+1}, \bar{u}_{3*}^{n+1})$, Δt is the time step, $\partial\Omega$ denotes the boundary and Ω denotes the interior of the domain excluding the boundaries. Solution of (20) is facilitated by boundary conditions satisfied by the velocity field at time t_{n+1}, $\bar{\boldsymbol{u}}^{n+1}$, imposed on the intermediate solution at time t_{n+1}, $\bar{\boldsymbol{u}}_*^{n+1}$. Our horizontal spatial discretization to be described later is spectral, thus all variables satisfy periodicity in x_1 and x_2. The spatial discretization in the vertical direction (i.e. in x_3) uses high-order compact finite differences, thereby permitting Dirichlet, Neumann or periodic boundary conditions at the top and bottom bounding surfaces of our flow domains. For all our cases with non-periodic boundary conditions in x_3 (i.e. Neumann or Dirichlet boundary conditions) the boundary condition on the x_3 component of the velocity, $\bar{u}_3$, is zero. This condition is not enforced on the intermediate velocity $\bar{u}_{3*}^{n+1}$. Instead, following Slinn and Riley (1998), Eq. (20) is solved on the top and bottom boundaries using one-sided vertical derivative approximations, giving rise to a solution for $\bar{u}_{3*}^{n+1}$ at these boundaries. The solution for $\bar{u}_{3*}^{n+1}$ is retained for later use in the boundary condition for pressure. Information regarding our prescription of one-sided and central derivative approximations in the vertical direction are given in Appendix.

The intermediate solution, $\bar{\boldsymbol{u}}_*^{n+1}$, obtained from (20) with appropriate boundary conditions does not satisfy the divergence-free condition. To enforce this condition, the following Poisson's equation for pressure is solved:

$$\boldsymbol{\nabla}^2(\Delta \bar{p}^{n+1}) = \frac{1}{\Delta t}\boldsymbol{\nabla} \cdot \bar{\boldsymbol{u}}_*^{n+1} \quad \text{in } \Omega + \partial\Omega,$$
$$\frac{\partial \Delta \bar{p}^{n+1}}{\partial x_3} = \frac{1}{\Delta t}\bar{u}_{3*}^{n+1} \quad \text{on } \partial\Omega$$
$$\bar{p}^{n+1} = \bar{p}^n + \Delta \bar{p}^{n+1} \quad \text{in } \Omega + \partial\Omega.$$
(21)

The divergence-free velocity is finally obtained as

$$\bar{\boldsymbol{u}}^{n+1} = \bar{\boldsymbol{u}}_*^{n+1} - \Delta t \, \boldsymbol{\nabla}(\Delta \bar{p}^{n+1}) \quad \text{in } \Omega + \partial\Omega.$$
(22)

As mentioned earlier, while solving Eq. (20), the component of the intermediate velocity normal to the bottom and top boundaries (i.e. $\bar{u}_{3*}^{n+1}$ on $\partial\Omega$) is not specified and thus kept free as given by the solution of (20). In turn, this free velocity affects the solution of Poisson's equation for pressure through the boundary condition in

(21). As discussed by Slinn and Riley (1998), this is required to ensure convergence of the method. However, at the end of the time step, when the final velocity is computed via (22), $\bar{u}_3^{n+1}$ is set to zero on $\partial\Omega$, thus satisfying the true boundary condition. Validation studies shown in Appendix along with the theoretical results of Fringer et al. (2003) have demonstrated that this splitting of the momentum and continuity equation together with the chosen Adams–Bashforth and Crank–Nicholson schemes is second-order accurate in time for finite Reynolds number.

Finally, the temperature equation is discretized in similar fashion as the momentum equation. Let

$$\mathscr{H}(\bar{u}_k, \bar{\theta}) = \left(\bar{u}_j + \frac{1}{La_t}\phi_j\right)\frac{\partial\bar{\theta}}{\partial x_j} - \frac{\partial\lambda^{sgs}}{\partial x_j},$$
(23)

discretizing $\mathscr{H}$ using the Adams–Bashforth scheme as

$$\mathscr{N}(\bar{u}_k^n, \bar{\theta}^n, \bar{u}_k^{n-1}, \bar{\theta}^{n-1}) = \frac{3}{2}\mathscr{H}(\bar{u}_k^n, \bar{\theta}^n) - \frac{1}{2}\mathscr{H}(\bar{u}_k^{n-1}, \bar{\theta}^{n-1}),$$
(24)

and the molecular diffusion term using the Crank–Nicholson scheme, the temperature equation becomes

$$\left(\frac{1}{\Delta t} - \frac{1}{2RePr}\boldsymbol{\nabla}^2\right)\Delta\bar{\theta}^{n+1} = -\mathscr{N}(\bar{u}_k^n, \bar{\theta}^n, \bar{u}_k^{n-1}, \bar{\theta}^{n-1}) + \frac{1}{RePr}\boldsymbol{\nabla}^2\bar{\theta}^n \quad \text{in } \Omega,$$
$$\bar{\theta}^{n+1} = \bar{\theta}^n + \Delta\bar{\theta}^{n+1} \quad \text{in } \Omega + \partial\Omega,$$
(25)

Depending on the problem, Dirichlet or Neumann boundary conditions in the vertical direction can be assigned to the filtered temperature $\bar{\theta}$.

3.2. Spatial discretization

The spatial discretization is hybrid, making use of fast Fourier transforms in the horizontal directions (x_1 and x_2) and high-order finite differences in the vertical direction (x_3). Taking the two-dimensional Fourier transform of the semi-discrete momentum equation in (20) and denoting a Fourier transformed quantity with an over-hat, $\hat{\cdot}$, leads to

$$\left(\frac{1}{\Delta t} + \frac{1}{2Re}|\boldsymbol{k}_h|^2 - \frac{1}{2Re}\frac{\delta^2}{\delta x_3^2}\right)\widehat{\Delta\bar{\boldsymbol{u}}}_*^{n+1} = -\widehat{\boldsymbol{N}}(\bar{\boldsymbol{u}}^n, \bar{\boldsymbol{u}}^{n-1}) - \boldsymbol{\nabla}_s\,\widehat{\bar{p}}^n$$
$$+ \frac{1}{Re}\left\{-|\boldsymbol{k}_h|^2 + \frac{\delta^2}{\delta x_3^2}\right\}\widehat{\bar{\boldsymbol{u}}}^n \quad \text{in } \Omega,$$
$$\widehat{\bar{\boldsymbol{u}}}_*^{n+1} = \widehat{\bar{\boldsymbol{u}}}^n + \widehat{\Delta\bar{\boldsymbol{u}}}_*^{n+1} \quad \text{in } \Omega,$$
(26)

where $\boldsymbol{k}_h = k_1\boldsymbol{e}_1 + k_2\boldsymbol{e}_2$ and k_1 (viz. $\boldsymbol{e}_1$) and k_2 (viz. $\boldsymbol{e}_2$) are the wavenumbers (viz. unit vectors) in the x_1 and x_2 directions, respectively. The operator $\delta/\delta x_3$ denotes the finite-difference approximation of $\partial/\partial x_3$ and $\boldsymbol{\nabla}_s = (ik_1, ik_2, \delta/\delta x_3)$. Further information regarding the finite-difference operators can be found in Appendix.

Approximation of vertical (x_3) derivatives in (26) via higher order compact finite differences leads to a linear system of the form $\boldsymbol{A}_{(k_1,k_2)}^i \boldsymbol{x}_{(k_1,k_2)}^i = \boldsymbol{b}_{(k_1,k_2)}^i$ for each intermediate velocity increment, $\widehat{\Delta\bar{u}}_{i*}^{n+1}$, at each horizontal wavenumber pair (i.e. at each k_1 and k_2 pair). One-sided derivative approximations are used at and near boundaries in x_3. In the resulting system, $\boldsymbol{A}$ is a matrix and $\boldsymbol{x}$ and $\boldsymbol{b}$ are vectors. Vector $\boldsymbol{x}$ contains the solution $\left(\widehat{\Delta\bar{u}}_{i*}^{n+1}\right)$ at each x_3 grid level. Matrix $\boldsymbol{A}$ is $(n_z + 1) \times (n_z + 1)$ and vectors $\boldsymbol{x}$ and $\boldsymbol{b}$ are $(n_z + 1) \times 1$, where $n_z + 1$ is the number of grid levels or grid points in x_3. The rows of the system correspond to the discretization of either the x_1, x_2 or x_3 momentum equation in (26) at each x_3 level. Rows 1 and $(n_z + 1)$ correspond to Eq. (26) at the bottom and top boundaries of the domain, respectively. However, if for example, a Dirichlet bottom boundary (BC) condition is applied, then the first row of $\boldsymbol{A}$ is replaced by vector $(1, 0, 0, \ldots, 0)$ and the first entry

of vector $\boldsymbol{b}$ is replaced by a 0, when solving the x_1 or x_2 momentum equation (i.e. when for $\bar{u}_{1*}^{n+1}$ and $\bar{u}_{2*}^{n+1}$). If a Neumann BC is applied, then the first row or equation in the linear system is replaced by the compact finite-difference approximation of the Neumann BC. As mentioned earlier, Dirichlet or Neumann BCs are never imposed on $\bar{u}_{3*}^{n+1}$, thus the first and last rows of the system always remain unchanged when solving the x_3 momentum equation. Finally, when periodic boundary conditions are applied in x_3, one-sided derivative approximations are not required to solve the momentum equation, as no boundaries are present and the domain wraps around itself. That is the solution at the first x_3-level (or the first equation of the system) is the same as the solution at the last x_3-level (or the last equation of the system).

Taking the Fourier transform of the temperature equation in (25), we have

$$
\left(\frac{1}{\Delta t} + \frac{1}{2RePr}|\boldsymbol{k}_h|^2 - \frac{1}{2RePr}\frac{\delta^2}{\delta x_3^2}\right)\widehat{\Delta\bar{\theta}}_*^{n+1} = -\widehat{\mathcal{N}}(\bar{u}_k^n, \bar{\theta}^n, \bar{u}_k^{n-1}, \bar{\theta}^{n-1})
$$
$$
+ \frac{1}{RePr}\left\{-|\boldsymbol{k}_h|^2 + \frac{\delta^2}{\delta x_3^2}\right\}\widehat{\bar{\theta}}^n \quad \text{in } \Omega,
$$
$$
\widehat{\bar{\theta}}_*^{n+1} = \widehat{\bar{\theta}}^n + \widehat{\Delta\bar{\theta}}_*^{n+1} \quad \text{in } \Omega.
$$
$$(27)$$

Dirichlet and Neumann boundary conditions for (27) are imposed similar to those in the momentum equation described earlier.

Taking the two-dimensional Fourier transform of Poisson's equation in (21) leads to

$$
\left(-|\boldsymbol{k}_h|^2 + \frac{\delta^2}{\delta x_3^2}\right)\widehat{\Delta\bar{p}}^{n+1} = \frac{1}{\Delta t}\left(ik_1\widehat{\bar{u}}_{1*}^{n+1} + ik_2\widehat{\bar{u}}_{2*}^{n+1} + \frac{\delta}{\delta x_3}\widehat{\bar{u}}_{3*}^{n+1}\right) \text{ in } \Omega + \partial\Omega,
$$
$$
\frac{\delta\widehat{\Delta\bar{p}}^{n+1}}{\delta x_3} = \frac{1}{\Delta t}\widehat{\bar{u}}_{3*}^{n+1} \quad \text{on } \partial\Omega,
$$
$$
\widehat{\bar{p}}^{n+1} = \widehat{\bar{p}}^n + \widehat{\Delta\bar{p}}^{n+1} \quad \text{in } \Omega + \partial\Omega.
$$
$$(28)$$

The velocity at time step $n + 1$ becomes

$$
\widehat{\bar{u}}_1^{n+1} = \widehat{\bar{u}}_{1*}^{n+1} - i\,\Delta t\,k_1\widehat{\Delta\bar{p}}^{n+1} \quad \text{in } \Omega + \partial\Omega,
$$
$$
\widehat{\bar{u}}_2^{n+1} = \widehat{\bar{u}}_{2*}^{n+1} - i\,\Delta t\,k_2\widehat{\Delta\bar{p}}^{n+1} \quad \text{in } \Omega + \partial\Omega,
$$
$$
\widehat{\bar{u}}_3^{n+1} = \widehat{\bar{u}}_{3*}^{n+1} - \Delta t\frac{\delta}{\delta x_3}\widehat{\Delta\bar{p}}^{n+1} \quad \text{in } \Omega + \partial\Omega.
$$
$$(29)$$

The nonlinear advection terms in Eqs. (18) and (23) generate scales at high wavenumbers (i.e. small scales) unresolvable by the grid. This effect is reflected through an accumulation of energy at the smallest resolved scales, often referred to as aliasing. In order to prevent this spurious accumulation, de-aliasing is performed using the well-known 3/2-rule in the horizontal directions. The high-order (fourth-order) filter discussed by Slinn and Riley (1998) (see Appendix) is applied in the vertical direction to the advection terms at each time step in order to attenuate the spurious high wavenumber energy accumulation while preserving the more energetic scales at lower wavenumber and the high-order accuracy of the spatial scheme.

Next we describe our experiences in applying the previously described discretization to shallow water and deep water surface mixed layer flows.

4. Numerical results

4.1. Langmuir supercells in shallow water

Historically, Langmuir cells have been measured within the upper ocean surface mixed layer in deep water far above the bot-

tom. Recently, Gargett et al. (2004) and Gargett and Wells (2007) reported detailed acoustic Doppler current profiler (ADCP) measurements of Langmuir cells engulfing the entire water column lasting as long as 18 h in a shallow water region off the coast of New Jersey. Measurements were made at Rutgers' LEO15 cabled observatory in 15 m depth water. Gargett et al. (2004) denoted the observed full-depth cells as Langmuir supercells (LSC) because of their important role as vectors for the transport of sediment and bioactive material on shallow shelves.

Using the discretization previously described, Tejada-Martínez and Grosch (2007) performed LES-NWR of a finite-depth, homogeneous, wind-driven shear current with LSC under wind and wave forcing representative of the conditions during the LEO15 LSC event. A sketch of the domain is given in Fig. 1a. The computational domain was taken $4\pi\delta$ long in the downwind direction, $8\pi\delta/3$ wide in the crosswind direction and 2δ deep, sufficient for the resolution of one LSC, where δ is half-depth, as noted earlier. The grid comprised 32 dealiased modes in the x_1 and x_2 (horizontal) directions and 97 points in the x_3 (vertical) direction (i.e. ($32 \times 32 \times 96$)). Henceforth the number of horizontal grid points given in all computations presented will correspond to the number of de-aliased Fourier modes. Furthermore, the C–L vortex force was set with turbulent Langmuir number (La_t) of 0.7 and dominant surface wave wavelength (λ) of $6H$ where H is depth. The no-slip condition was prescribed at the bottom of the domain and a wind stress (given as $\tau_s = \rho_o u_\tau^2$, where u_τ is the wind stress friction velocity) was prescribed at the top of the domain in the x_1-direction. In dimensionless terms, application of this wind stress results in $d\bar{u}_1/dx_3 = Re$ and $d\bar{u}_2/dx_3 = 0$ at the surface.

Predictions from the LES compared favorably with the in-water measurements. The reader is directed to the companion articles of Gargett and Wells (2007) and Tejada-Martínez and Grosch (2007) for details of this comparison and the computational setup. Here we point to some aspects of the LES relevant to our discussion in the Section 1. We note that the LES-NWR was made at a much low-
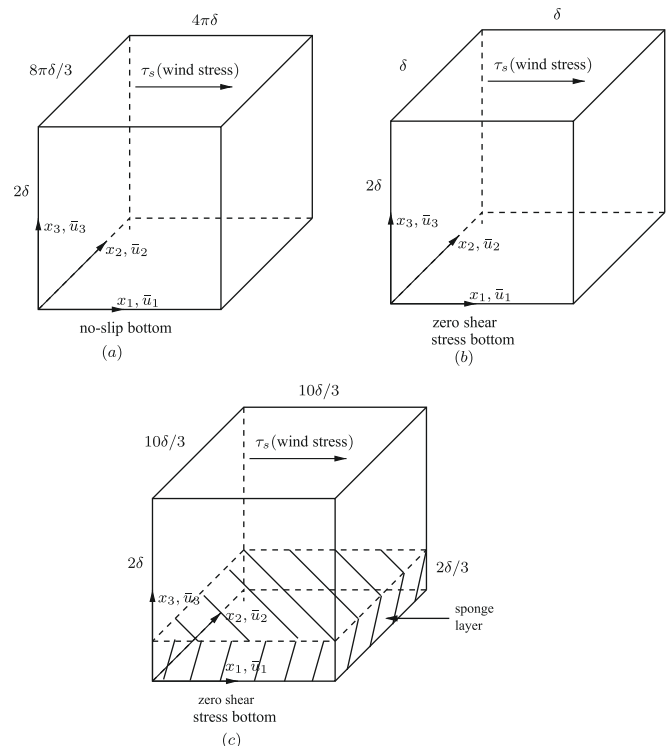
Fig. 1. Sketch of domains for (a) LES-NWR of LSC in shallow water, (b) LES-NWM of an unstratified Ekman layer and (c) LES-NWM of a stratified Ekman layer with LC.
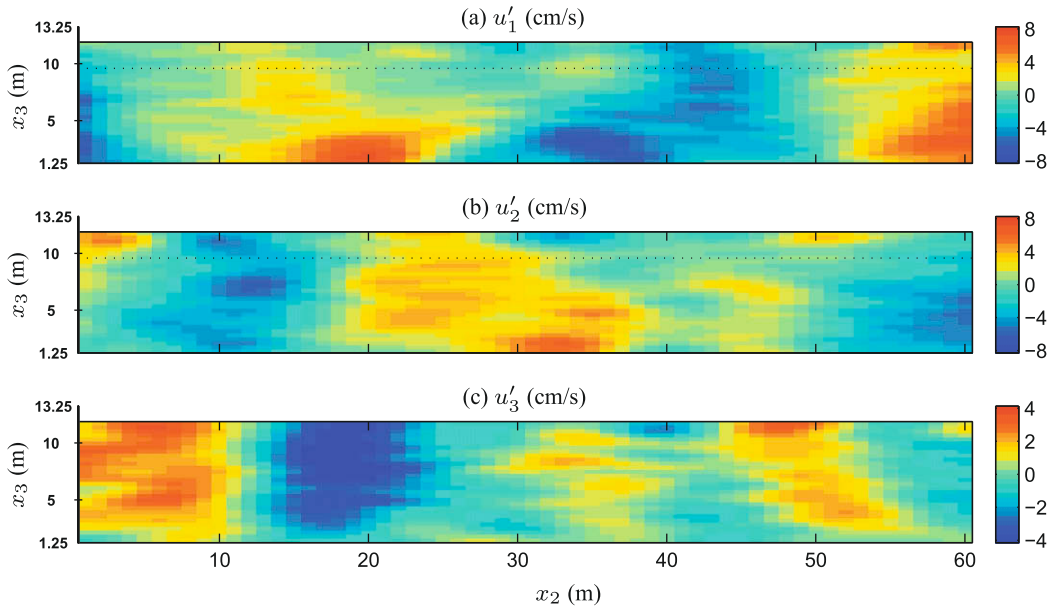
Fig. 2. Instantaneous fluctuating downwind, crosswind and vertical velocity components as recorded in the field (at LEO15) by an ADCP while Langmuir supercells were being advected in the crosswind direction. The fluctuations reveal one Langmuir supercell. The lowermost 1.25 m were not measurable by the ADCP; measurements of u_1' and u_2' above $\sim$10 m (denoted by a dashed line) were affected by sidelobe contamination.

er Reynolds number ($Re_\tau = 395$ based on wind friction velocity and half-depth) than that of the field observations ($Re_\tau = O(50,000)$). In spite of this, the LES was able to capture the main features of a Langmuir supercell manifested as a secondary, coherent turbulent structure advected by the mean shear flow. Figs. 2 and 3 compare the observed structure with the LES-computed structure. Notice that in both, field observation and LES, the downwelling region (i.e. the region of negative vertical velocity fluctuations) of the cell coincides with a region of positive downwind velocity fluctuations. Furthermore, the region of positive downwind velocity fluctuations in the LES is characterized by near-bottom intensification similar to the field-measured structure. The LES variables were made dimensionless with the wind stress friction velocity, and

when scaled by the field-measured wind stress friction velocity, the magnitudes of the LES-predicted velocity fluctuations are in close agreement with those measured in the field. A similar agreement is also seen in terms of the magnitude of the Reynolds stress components (not shown).

In addition to the secondary structure previously described, the full turbulent structure computed in the LES is in agreement with the field-measured structure. This is reflected through the depth-trajectory of the second and third invariants of the Reynolds stress anisotropy tensor which must lie inside the Lumley triangle (Pope, 2000) for all realizable turbulent flows. As seen in Fig. 4, the map of the invariants computed in the LES agrees well with the map of the invariants measured in the field, especially in the lower third por-
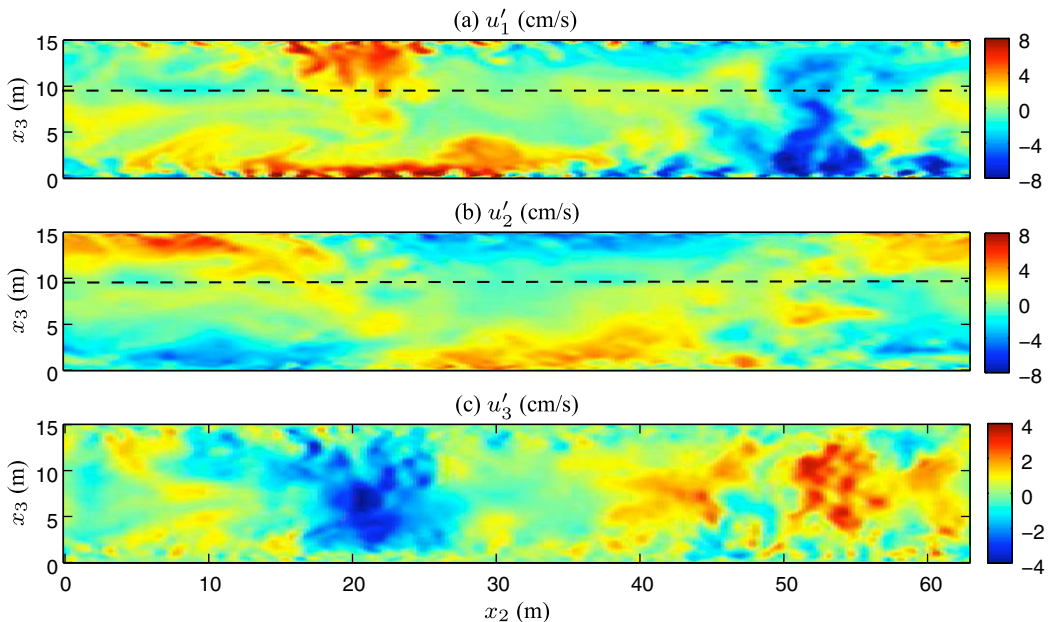
Fig. 3. Instantaneous fluctuating downwind, crosswind and vertical velocity components measured in LES. Computational velocities have been made dimensional with the wind stress friction velocity recorded in the field during the observations of Gargett and Wells (2007).
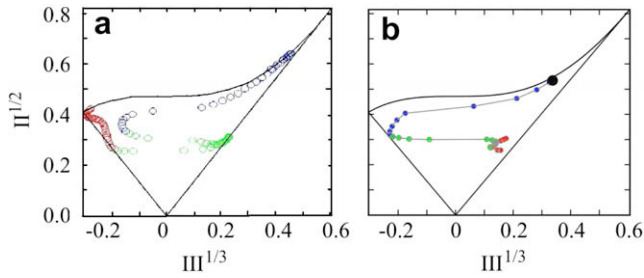
Fig. 4. Trajectory of Lumley invariant maps in (a) LES and (b) observations of Langmuir supercells. Blue symbols denote trajectory of map in the lower third of the water column, green symbols denote the trajectory in the middle third and the red symbols denote the trajectory in the upper third. (For interpretation of color mentioned in this figure the reader is referred to the web version of the article.)

tion of the water column. In this region, the map lies in the interior of the triangle in proximity to the upper curved edge. This is indicative of the dominant, near-bottom two-component turbulent structure of the flow characterized by strong downwind velocity fluctuations generated by the mean shear and strong crosswind velocity fluctuations generated by the bottom convergences and divergences of the cells. In the absence of LSC and thus strong

crosswind fluctuating velocity component, the map would lie along the right-hand side edge of the triangle, indicative of shear-dominated turbulence.

Overall, agreement between the observed and computed turbulent structures is primarily within the lower half of the water column. Comparison in the upper half is more difficult as uncertainties in ADCP measurements are prominent, especially in the upper 3–5 m of the water column (Gargett and Wells, 2007). Furthermore, this region is expected to be influenced by wave-breaking, which the LES is not capable of representing.

Fig. 5a shows shear (1–3) components of viscous, Reynolds and SGS stress in LES with and without LSC (i.e. without wave effects). In both simulations, the SGS stress is given by the dynamic Smagorinsky model in (9) and (10). The SGS stress goes to zero at the bottom and at the surface of the domain following the behavior of the model coefficient in (10). At the surface, the viscous shear stress matches the wind stress thereby transmitting momentum flux from the surface to the interior. Once in the interior, the flux is transmitted by the Reynolds shear stress to depths where viscous effects are negligible.

Fig. 5b shows mean downwind velocity in LES with and without LSC. These mean velocity profiles demonstrate the impact of LSC on the viscous wall region and the log-layer region. The presence of LSC disrupts the typical log-law behavior of the mean velocity
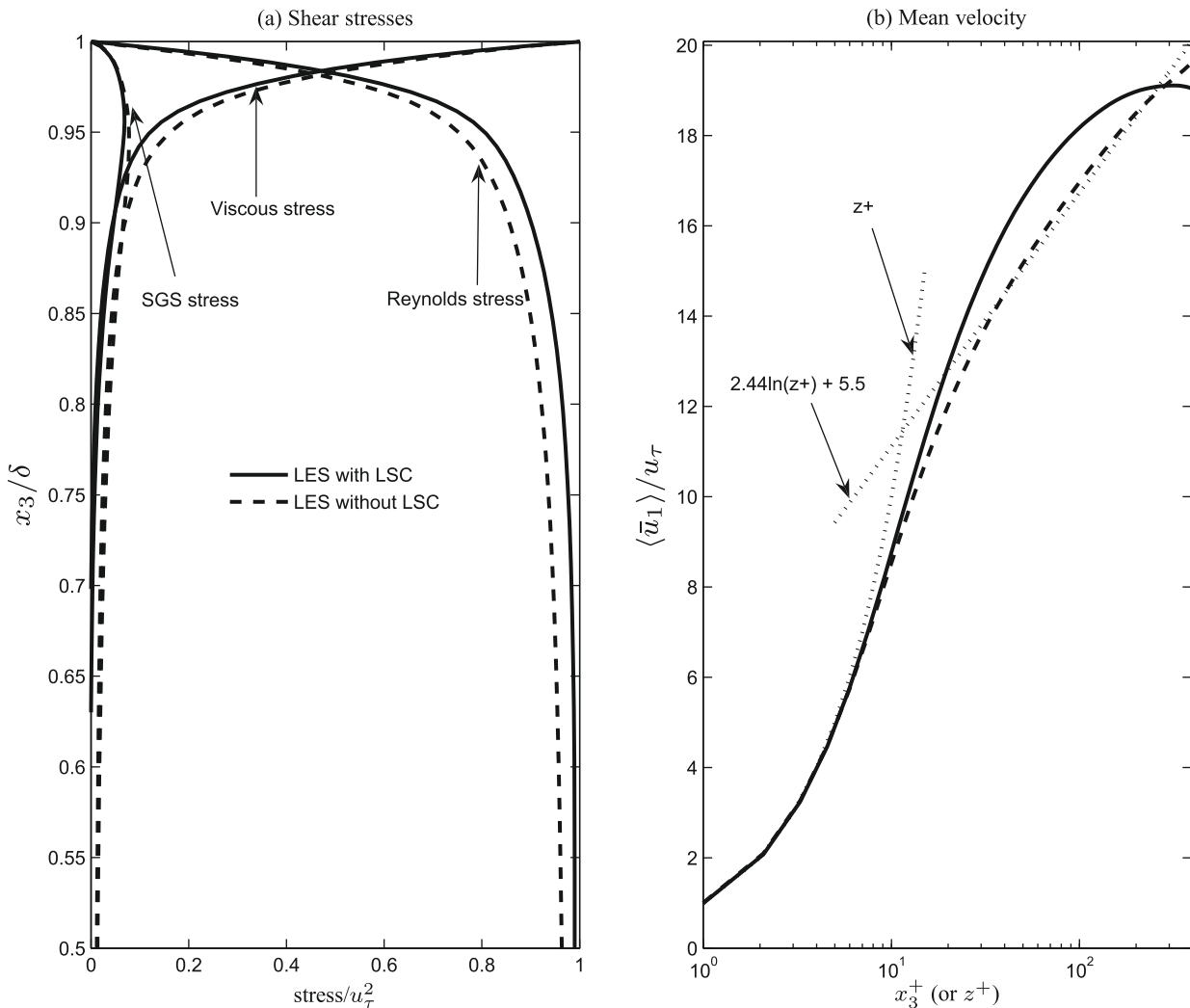
Fig. 5. (a) Shear stress components in the upper fourth of the water column and (b) mean velocity in the lower half of the water column in LES of Langmuir supercells. The computational domain extends from $x_3/\delta = -1$ to $x_3/\delta = 1$. Furthermore, $x_3^+ = (x_3/\delta + 1)Re_\tau$.

inducing what resembles a law of the wake-like behavior. The law of the wake in traditional boundary layers has been attributed to large-scale turbulent mixing (Coles, 1956). LSC enhances this mixing and, as seen in Fig. 5b, generates a large wake region stretching down through the would-be log-layer region and into the buffer region. Note that our LES of the flow without LSC yields a clear log-law region. Thus, the previously described disruption of the log-layer in the presence of LSC is strictly due to C–L vortex forcing.

Further evidence of disruption of the log-layer by LSC comes from the analysis of turbulent velocity variances measured during the LSC event at LEO15 and a more recent event measured at the Navy's R2 tower on the Goergia shelf (Gargett and Savidge, 2008). Both measurements were made under similar wind and wave forcing conditions but different tidal forcing condition. Under a strong tidal current at R2, the near-constancy of the turbulent kinetic energy (TKE) in the lower third portion of the water column was indicative of a bed stress log-layer. However, a similar near-constancy of TKE was noticeably absent from the LEO15 LSC event, characterized by a much weaker tidal current. This non-constancy of TKE was also the case in our LES of LSC guided by the LEO15 measurements (Tejada-Martínez and Grosch, 2007).

4.2. Unstratified Ekman layer

In this subsection we present results from LES-NWM of an unstratified, surface wind-driven Ekman layer. We will focus on the performance of the dynamic Smagorinsky parametrization in (9)–(12) and the Smagorinsky parametrization based on similarity in (9) and (17) (henceforth referred to as the Smagorinsky–Mason parametrization).

The computational domain for the Ekman layer is taken to be $L_1 = \delta$ long in the downwind direction and $L_2 = \delta$ wide in the crosswind direction, following the simulation of Zikanov et al. (2003) (see Fig. 1b). In the vertical direction the domain extends from 0 to 2δ, thus the dimensionless vertical coordinate extends from $x_3/\delta = 0$ to $x_3/\delta = 2$. The grid consists of $(32 \times 32 \times 129)$ points. A hyperbolic stretching function is employed in order to cluster more grid points near the surface (around $x_3 = 2\delta$) where velocity gradients are expected to be strongest. With this stretching, at the bottom of the domain the grid cell aspect ratio is $\Delta_3/\Delta_1 \approx 0.75$ varying down to $\Delta_3/\Delta_1 \approx 0.2$ at the surface, where Δ_i is the grid spacing in the ith direction. We have excluded the C–L vortex term appearing in the momentum equation, thereby excluding wave effects, and the Rossby number is $Ro = 1$.

The downwind (x_1) and crosswind (x_2) directions are homogeneous, thus periodic boundary conditions are taken in these directions. At the bottom of the Ekman layer ($x_3 = 0$), we impose zero normal velocity, that is $\{u_3\}_{x_3=0} = 0$ and zero tangential stress, that is

$$\left\{\bar{\tau}_{13}^{sgsd}\right\}_{x_3=0} = 0 \quad \text{and} \quad \left\{\bar{\tau}_{23}^{sgsd}\right\}_{x_3=0} = 0. \tag{30}$$

At the surface ($x_3 = 2\delta$), we impose zero normal velocity (i.e. $\{u_3\}_{x_3=2\delta} = 0$). Furthermore, the 1–3 component of the SGS stress is set equal to a specified wind stress, $\tau_s \equiv \rho_o u_\tau^2$ in the x_1 direction, while the 2–3 component of the SGS stress is set equal to zero. In dimensionless form these conditions become

$$\left\{\bar{\tau}_{13}^{sgsd}\right\}_{x_3=2\delta} = 1 \quad \text{and} \quad \left\{\bar{\tau}_{23}^{sgsd}\right\}_{x_3=2\delta} = 0. \tag{31}$$

Note that the simulation methodology chosen is LES-NWM for which the SGS stress matches the surface stress prescribed at the boundaries. This is in contrast to the LES-NWR of LSC described earlier, in which the molecular viscous stress matches the surface stress at the surface and the SGS stress decays to zero.

For all Ekman layer simulations (stratified and unstratified), regardless of the SGS model (dynamic Smagorinsky or Smagorin-

sky–Mason), we resort to similarity theory to impose control of the solution at the surface together with explicit use of Eq. (9). Following similarity theory (reviewed by Lewis (2005)) and the surface boundary condition $\bar{u}_3 = 0$ applied to Eq. (9), at the surface

$$\left\{\tau_{13}^{sgsd}\right\}_{x_3=2\delta} \approx (C_s\overline{\Delta})^2_{x_3=2\delta}\left(\frac{d\bar{u}_1}{dx_3}\right)^2_{x_3=2\delta}, \tag{32}$$

As noted by Eq. (31), $\tau_{13}^{sgsd} = 1$ at the surface. Using this condition with Eq. (32) mentioned above, we may solve for $d\bar{u}_1/dx_3$ at the surface:

$$\left(\frac{d\bar{u}_1}{dx_3}\right)_{x_3=2\delta} = \frac{1}{(C_s\overline{\Delta})_{x_3=2\delta}}, \tag{33}$$

where $(C_s\overline{\Delta})_{x_3=2\delta}$ is obtained by evaluating the similarity equation in (17) at the surface ($z = 0$). The remaining boundary conditions on solution derivatives are taken as $d\bar{u}_2/dx_3 = 0$ at the surface and $d\bar{u}_1/dx_3 = d\bar{u}_2/dx_3 = 0$ at the bottom which also follow from the boundary conditions on τ_{ij}^{sgsd} appearing in Eqs. (30) and (31) and the use of (9).

Following Zikanov et al. (2003) we employ the following decomposition of the instantaneous velocity $\bar{u}_i$:

$$\bar{u}_i = U_i(x_3, t) + \bar{u}_i', \tag{34}$$

where $U_i = \langle\bar{u}_i\rangle$ and $\langle\cdot\rangle$ denotes averaging over the horizontal (homogeneous) directions (x_1 and x_2) (i.e. the horizontal average). The instantaneous bulk velocity is defined as

$$U_i^b(t) = \frac{1}{2}\int_{x_3=0}^{x_3=2\delta} U_i(x_3, t)dx_3. \tag{35}$$

Fig. 6 shows the x_1 and x_2 bulk velocity components during our simulation. These components exhibit the undamped oscillation discussed by Lewis and Belcher (2004). Lewis and Belcher analytically solved the unsteady, linearized, wind-driven, finite-depth Ekman layer equations with constant eddy-viscosity. Note that their eddy-viscosity parameterizes all of the turbulence and is not the same as the eddy-viscosity in our LES. They solved two separate problems each characterized by different boundary conditions at the bottom of the domain: (1) $\partial u_1/\partial x_3 = \partial u_2/\partial x_3 = 0$ at $x_3 = 0$ and (2) $u_1 = u_2 = 0$ at $x_3 = 0$. The first condition is the same as in our simulation. Condition (2) leads to solutions composed of a steady-state component plus a damped temporal oscillatory component. As the name suggests, the damped component decays in time, thus eventually the solution becomes purely steady. Condition (1) leads to a solution composed of a steady-state component plus an undamped temporal oscillatory component. This undamped, the so-called, inertial oscillation remains part of the solution for all times, a characteristic exhibited by our numerical solution in Fig. 6. The undamped oscillations in U_1^b and U_2^b have a period of $2\pi Ro$ consistent with the non-dimensionalized version of the solution of Lewis and Belcher (2004) (Eq. (17), page 322 of their paper). Furthermore, U_1^b and U_2^b are out of phase with each other by $\pi/2$, consistent with the result of Lewis and Belcher (2004).

Taking the horizontal average of the x_1 and x_2 momentum equations in (1) excluding the buoyancy force and the C–L vortex force (i.e. letting $La_t = \infty$) and letting $Re = \infty$ leads to

$$\frac{\partial U_1}{\partial t} = -\frac{\partial\langle\bar{u}_1'\bar{u}_3'\rangle}{\partial x_3} + \frac{\partial\langle\tau_{13}^{sgsd}\rangle}{\partial x_3} + \frac{1}{Ro}U_2, \tag{36}$$

and

$$\frac{\partial U_2}{\partial t} = -\frac{\partial\langle\bar{u}_2'\bar{u}_3'\rangle}{\partial x_3} + \frac{\partial\langle\tau_{23}^{sgsd}\rangle}{\partial x_3} - \frac{1}{Ro}U_1, \tag{37}$$

respectively, where $\langle\bar{u}_i'\bar{u}_j'\rangle$ is the instantaneous resolved Reynolds stress. The flow under consideration is steady in a statistical sense
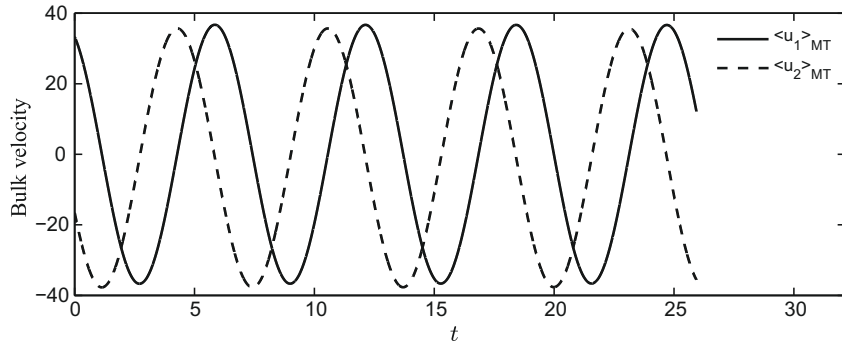
Fig. 6. Bulk downwind velocity, U_1^b, and bulk crosswind velocity, U_2^b, in an unstratified Ekman layer.

if averaged over times spanning M periods, MT, of the inertial oscillation, where $M = 1, 2, 3, \ldots$. Averaging (36) and (37) over M periods leads to $\langle \partial \bar{u}_1 / \partial t \rangle_{MT} = 0$ and $\langle \partial \bar{u}_2 / \partial t \rangle_{MT} = 0$ and thus

$$\frac{1}{Ro} \langle u_2 \rangle_{MT} = \frac{\partial \langle \bar{u}_1' \bar{u}_3' \rangle_{MT}}{\partial x_3} - \frac{\partial \langle \tau_{13}^{sgsd} \rangle_{MT}}{\partial x_3}, \tag{38}$$

and

$$-\frac{1}{Ro} \langle u_1 \rangle_{MT} = \frac{\partial \langle \bar{u}_2' \bar{u}_3' \rangle_{MT}}{\partial x_3} - \frac{\partial \langle \tau_{23}^{sgsd} \rangle_{MT}}{\partial x_3}, \tag{39}$$

respectively, where $\langle \cdot \rangle_{MT}$ denotes averaging over horizontal directions and over a time interval equal to MT. Integrating (38) and (39) leads to

$$\frac{1}{Ro} \int_0^{2\delta} \langle u_2 \rangle_{MT} dx_3 = -\left\{ \left\langle \tau_{13}^{sgsd} \right\rangle_{MT} \right\}_{x_3 = 2\delta}, \tag{40}$$

and

$$-\frac{1}{Ro} \int_0^{2\delta} \langle u_1 \rangle_{MT} dx_3 = 0, \tag{41}$$

respectively.

Next we compare results from LES using the dynamic Smagorinsky model (DSM), given by (9)–(12), and from LES using the Smagorinsky–Mason model (SMM), given by (9) and (17). In both simulations, the global conservation condition in (41) is satisfied up to within single precision machine epsilon. In the LES with SMM, the global conservation condition in (40) is satisfied up to 1.2% error. However, in the LES with DSM, this condition is only satisfied up to 26% error (while the simulation of Zikanov et al. (2003), also using the DSM, satisfied this condition up to 4% error). The source of this error will be discussed in detail further below.

Figs. 7–10 show results from simulations using DSM and SMM. Throughout the near-surface region, the 1–3 SGS stress given by the DSM is smaller than the 1–3 SGS stress given by the SMM. The reason for this can be traced to the model coefficient expressions in (10)–(12). As the surface is approached, the denominator in (10) becomes much larger than the numerator. Similar low values of the model coefficient have been obtained near the bottom surface in simulations of the atmospheric boundary layer (ABL) (Lund et al., 2003; Porté-Agel et al., 2000). Porté-Agel et al. (2000) attributed these low values to the fact that near the surface the dynamic procedure samples scales larger than the local integral scale thereby violating the scale-invariance assumption and leading to lower values of $\langle L_{ij} M_{ij} \rangle$. Under the scale-invariance assumption, the widths of the grid filter and the test filter are assumed to be within the inertial sub-range. In order to remedy this problem, Porté-Agel et al. (2000) introduced a scale-dependent dynamic procedure in which the scale-invariance assumption is not needed.

Values of the resulting dynamic model coefficient were observed to be larger than the values of the original dynamic model coefficient. An alternate approach was proposed by Lund et al. (2003). Following ideas proposed earlier by Sullivan et al. (1994), they represented the near-surface turbulence through an SGS parametrization consistent with similarity theory, similar to SMM. Lund et al. (2003) proposed a two-part SGS parameterization consisting of a blend between the DSM and a similarity-based model. Near the surface, the model based on similarity theory is active while decaying away from the surface as the inverse of the distance to the surface, similar to expression (17). Lund et al. (2003) identify the DSM as the LES part of their blended model and the model based on similarity theory as the Reynolds-averaged Navier–Stokes (or RANS) part.

Returning to our LES with the DSM, the dotted curve in Fig. 8a shows that the 1–3 component of the SGS stress close to the surface (at $x_3/\delta \approx 1.98$) is characterized by a non-monotonic (irregular) behavior. This irregularity induces a similar irregularity in u_3^{rms} (Fig. 7b) as well as in the 1–3 component of the resolved Reynolds stress (Fig. 8a) near the surface. Similar irregularities can also be observed in the results of Zikanov et al. (2003).

To understand the non-monotonic behavior of the 1–3 SGS component, we recall its form:

$$\tau_{13}^{sgsd} = (C_s \overline{\Delta})^2 |\bar{S}| \bar{S}_{13}. \tag{42}$$

Near the surface, the overall trend of τ_{13}^{sgs} is to increase in order to match the prescribed surface wind stress. However, as distance to the surface decreases, the decreasing trend of the dynamic model coefficient $(C_s \overline{\Delta})^2$ causes a small drop in the 1–3 SGS stress (Fig. 8a, dotted curve) interrupting the monotonic increase of the stress. As the distance to the surface continues to decrease, the 1–3 SGS stress recovers its increasing trend due to the dominant effect of the wall-normal gradient of the velocity (forming part of the $|\bar{S}|$ and $\bar{S}_{13}$ terms in (42)).

Although irregularities in the 1–3 SGS stress and the 1–3 Reynolds stress caused by the DSM are also seen in the simulations of Zikanov et al. (2003), these irregularities are more pronounced in our implementation. Furthermore, as discussed earlier, in our LES the global conservation statement in (40) is poorly satisfied up to 26% error while in the LES of Zikanov et al. (2003) this global conservation is satisfied more accurately up to 4% error.

In order to improve our LES results with the DSM we introduce a modification to our surface boundary condition. The modification is motivated by principles used to set the surface stress boundary condition in staggered grid formulations such as that of Zikanov et al. (2003). In such formulations, the horizontal momentum equations (characterized by 1–3 and 2–3 SGS stress components) are discretized at the so-called half-integer points located half-way between integer points along the vertical direction; the integer points correspond to the points on our non-staggered grid.
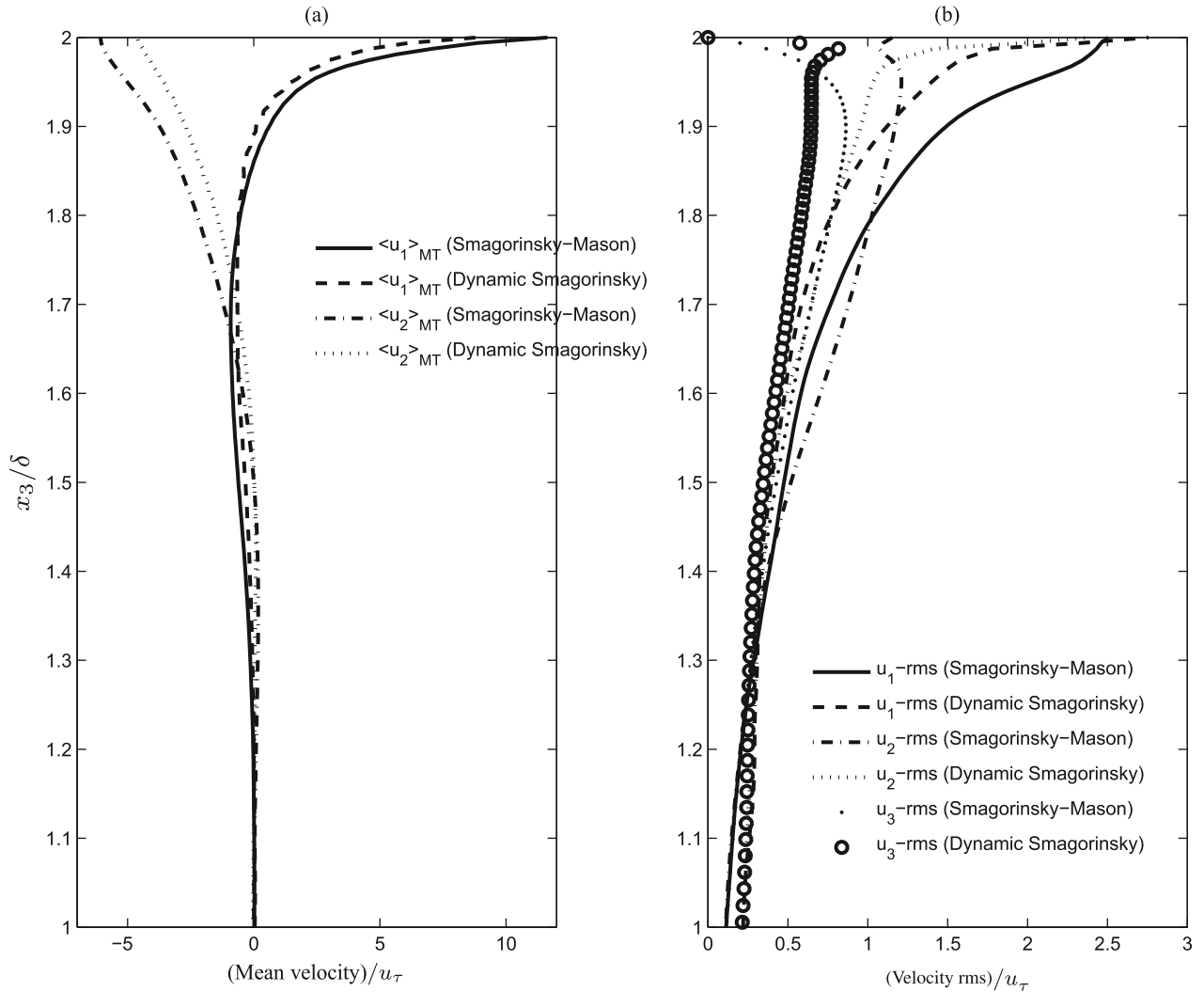
Fig. 7. (a) Mean velocity and (b) components of root mean square (rms) of velocity in unstratified Ekman layer. Time averaging was performed over $M = 5$ periods of inertial oscillation.

More precisely, the horizontal momentum equations are never treated at the surface; instead they are treated at locations $\Delta z/2$ below the surface, where Δz is the vertical distance between the surface and the first horizontal plane of grid (or integer) points below the surface. Thus, the boundary conditions on the 1–3 and 2–3 SGS stress components in (31) are assigned at a distance $\Delta z/2$ below the surface. This implies a constant stress layer spanning the region between the surface and the first plane of half integer points below the surface. This is consistent with the fact that the simulation does not resolve the inner layer surface region, but rather only resolves up to the log-layer region where the 1–3 stress is nearly constant and equal to the surface stress (Pope, 2000). Analogously, we postulate a similar constant stress layer in our LES, and the 1–3 stress boundary condition in (31) is prescribed at the surface and at the first horizontal plane of grid points below the surface in a Reynolds-average sense. The dimensionless, prescribed 1–3 SGS stress is obtained form:

$$-\langle \bar{u}_1' \bar{u}_3' \rangle_h + \tau_{13}^{sgsd} = 1, \qquad (43)$$

where $\langle \bar{u}_1' \bar{u}_3' \rangle_h$ denotes averaging the instantaneous quantity $\bar{u}_1' \bar{u}_3'$ over horizontal directions x_1 and x_2. Note that on the surface $\langle \bar{u}_1' \bar{u}_3' \rangle_h = 0$, thus $\tau_{13}^{sgsd} = 1$ just as in Eq. (31). On the horizontal plane of grid points below the surface $\tau_{13}^{sgsd} = 1 + \langle \bar{u}_1' \bar{u}_3' \rangle_h$. The effect of this

modification (denoted as BC2 in the figure legends) greatly improves results relative to the original boundary condition (denoted as BC1) in which the SGS stress is prescribed only at the surface. Figs. 9 and 10 compare results between the LES with BC1 and the LES with BC2. Irregularities present in the 1–3 SGS stress, 1–3 Reynolds stress and u_3^{rms} predicted in LES-BC1 are less pronounced than those in LES-BC2. Overall, the results obtained from LES-BC2 are in closer agreement with those obtained in LES of Zikanov et al. (2003). For example, the peak value of the 1–3 Reynolds stress and the mean crosswind velocity at the surface are closer to those presented by Zikanov et al. (2003).

In LES-BC2, the global conservation statement in (40) is satisfied up to within less than 5% in close agreement with the 4% reported in the LES of Zikanov et al. (2003). Recall that this error in LES-BC1 is much greater at 26%. As described earlier, nonlinear terms in the momentum equation are discretized in time with the second-order Adams–Bashforth scheme (AB2), which is unconditionally unstable for the treatment of a pure convective equation. Thus the error in Eq. (40) may be associated with instability of the AB2 scheme triggered by low values of the SGS stress. We have implemented the third-order Runge–Kutta (RK3) scheme described by Garg et al. (1997) (replacing the AB2 scheme) and tested it in LES-BC2. Unlike AB2, RK3 can be conditionally stable for a purely convective equation. The new simulation with RK3 was performed with the
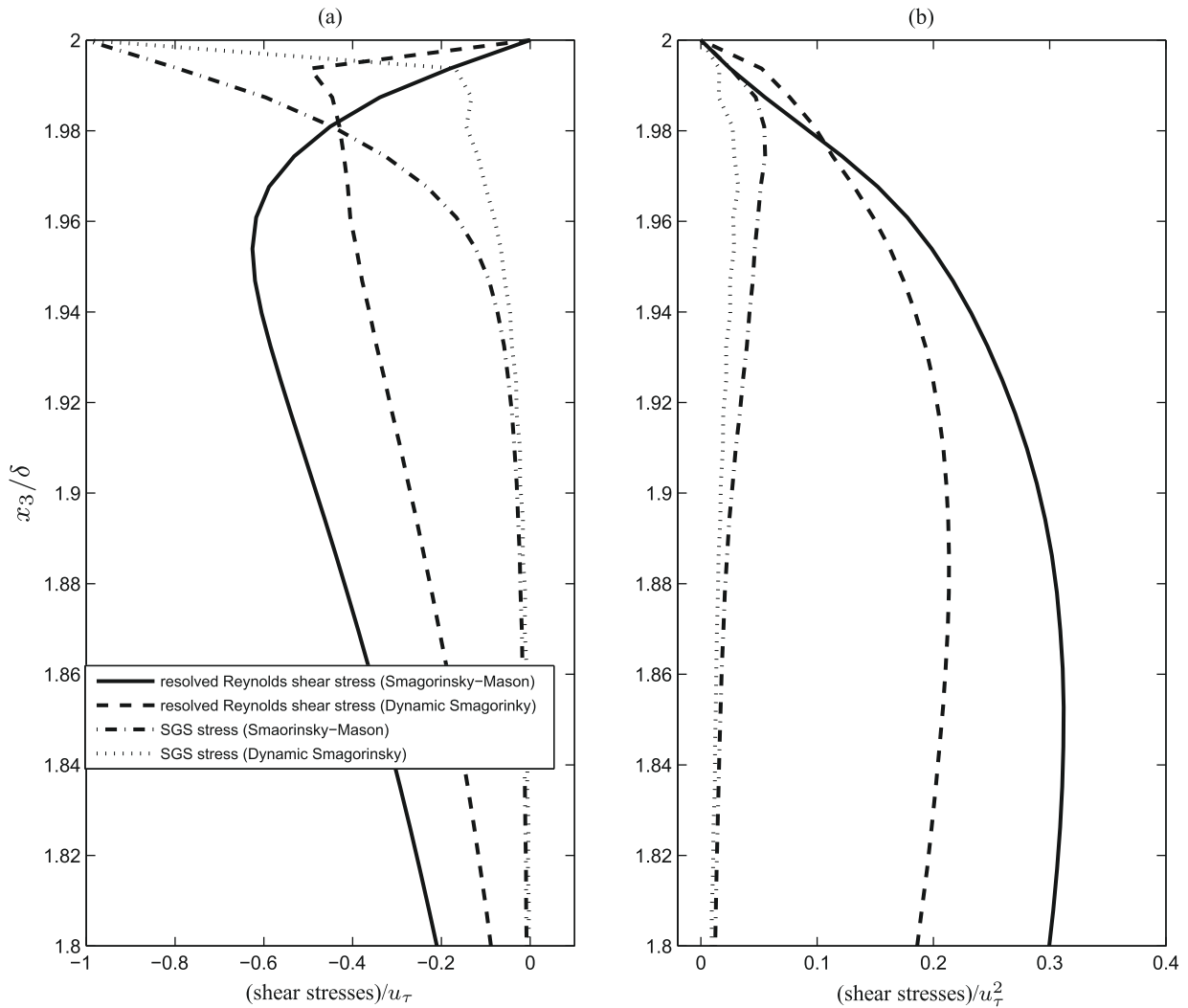
Fig. 8. Near-surface (a) downwind-vertical Reynolds and SGS shear stresses and (b) crosswind-vertical Reynolds and SGS shear stresses in an unstratified Ekman layer. Time averaging was performed over $M = 5$ periods of inertial oscillation.

same time step as the original simulation with AB2. RK3 scheme improved the satisfaction of the continuity equation by a factor of approximately 3 and reduced the error in Eq. (40) down to less than 1%. RK3 led to a slight increase in bulk crosswind mean velocity mainly by increasing the magnitude of the dimensionless crosswind mean velocity at the surface from approximately 5 (with Adams–Bashforth) to approximately 6, consistent with the reduction of the error in Eq. (40). Finally, RK3 led to negligible impact on velocity root mean squares and Reynolds stress components. We also tested RK3 in LES-BC1 and found a similar reduction of the error in the continuity equation, but did not obtain a reduction of the error in Eq. (40). The latter error was not reduced possibly due to the pronounced non-monotonic (irregular) behavior in the 1–3 component of the SGS stress in LES-BC1, described earlier, or the excessively low values of the SGS stress.

In summary, our non-staggered grid formulation has revealed the importance of the constant stress layer in DSM LES-NWM of the UOML and possibly of the ABL as well. Previous simulations have involved staggered grid formulations for which the constant stress layer is the only choice, thereby obscuring its effects. A number of researchers have reported difficulties with the DSM leading to a small 1–3 SGS stress component near the surface and thus a lack of sufficient turbulent kinetic energy dissipation. Our results demonstrate that this problem of the DSM is indeed more severe

than initially thought and is greatly alleviated by the constant stress layer.

4.3. Langmuir cells in a stratified turbulent Ekman layer

Here we review results from LES-NWM of a stratified Ekman layer flows with C–L vortex forcing generating LC. The SGS stress is parameterized with the SMM rather than the DSM for reasons to be explained later. Two simulations are reviewed. The first simulation (simulation 1) is performed with turbulent Langmuir number $La_t = 0.334$ (the same value used by Skyllingstad and Denbo (1995); henceforth SD95) and the second (simulation 2) is performed with $La_t = 0.3$ (the same value used by McWilliams et al. (1997)). The wavelength of the deep water waves represented by the C–L force is 60 m. In simulation 1, $Ro = 1$ and in simulation 2, $Ro = 1.3556$, the latter following McWilliams et al. (i.e. $f = 10^{-4}$ s^{-1}, corresponding to 45°N latitude). In both simulations the extent of the domain is 150 m in the downwind and crosswind directions and 90 m in the vertical. Note that in the figures shown further ahead and in the domain sketch of Fig. 1c these lengths are made dimensionless with the half-depth ($\delta = 45$ m), as described earlier. Both cases start from rest ($\bar{u}_i = \overline{\Pi} = 0$) and with suddenly imposed surface waves (represented via the C–L force) and wind stress in the x_1 direction with associated friction velocity
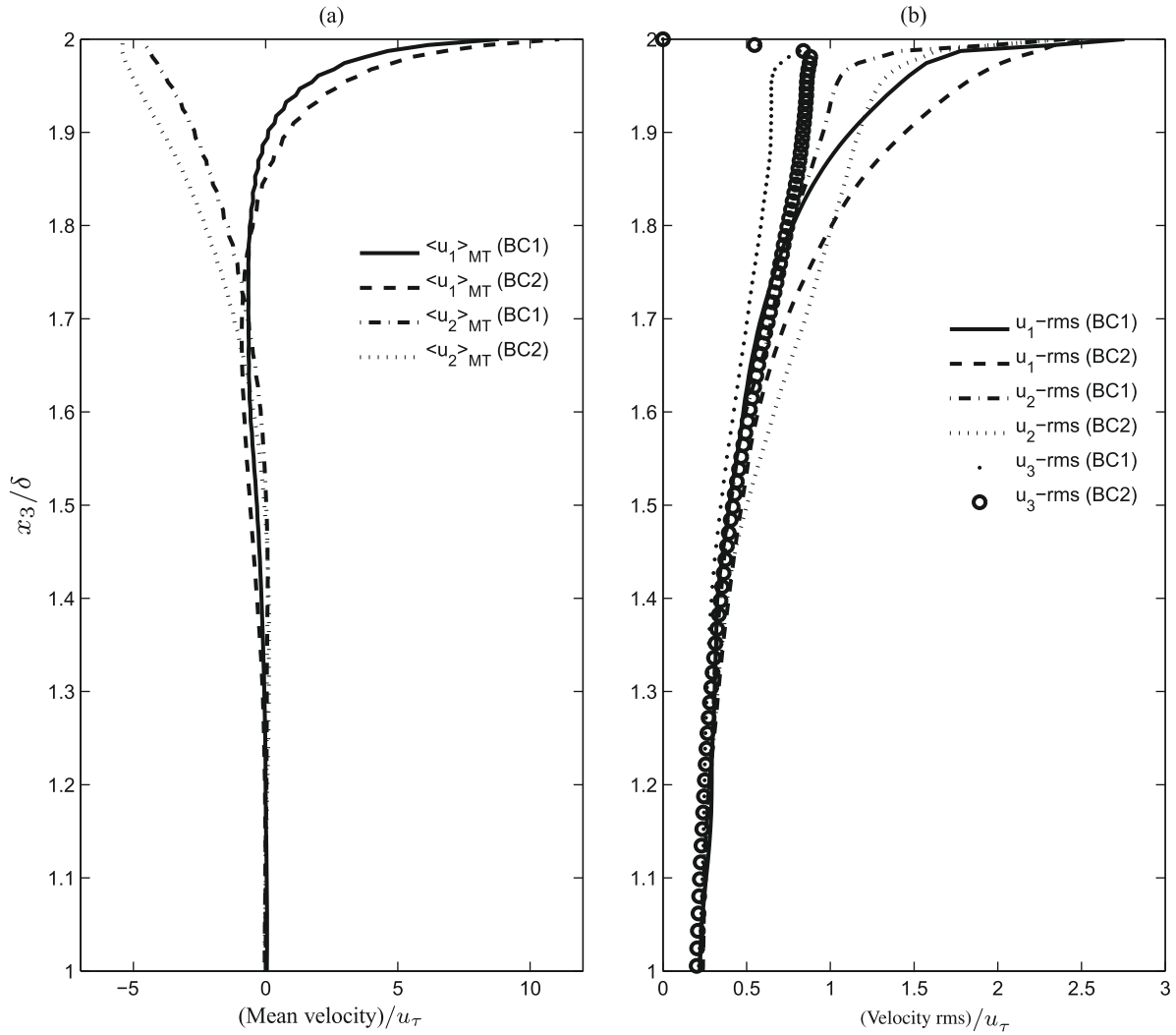
Fig. 9. (a) Mean velocity and (b) components of root mean square (rms) of velocity in unstratified Ekman layer. Time averaging was performed over $M = 5$ periods of inertial oscillation.

$u_\tau = 6.1 \times 10^{-3}$ m s^{-1}. Furthermore, both cases possess a constant initial temperature profile within the upper 33 m of the water column and a stable, linear profile in the lower 57 m. This stably stratified region is characterized by a buoyancy frequency of $N = 0.0044$ s^{-1}, corresponding to $(d\bar\theta/dx_3)_{x_3=0} = 0.01$ K m^{-1} and $\eta = 2 \times 10^{-4}$ K^{-1}. Using these values in the definition of the Richardson number in (8) we obtain $Ri = 1067.7$.

The boundary conditions for the flow variables are those described earlier in the LES of the unstratified Ekman layer. For temperature, at the bottom boundary we prescribe a fixed vertical gradient (i.e. $(d\bar\theta/dx_3)_{x_3=0}$). As we have non-dimensionalized temperature with $(d\bar\theta/dx_3)_{x_3=0}$, the vertical gradient of the dimensionless temperature at the bottom is simply $\partial\bar\theta/\partial x_3 = 1$. At the surface, the temperature gradient is obtained via the following condition

$$\left\{\frac{v_e}{Pr_t}\frac{\partial\bar\theta}{\partial x_3}\right\}_{x_3=2\delta} = \frac{Q}{C_p\rho_o u_\tau\delta}\left(\frac{d\bar\theta}{dx_3}\right)^{-1}_{x_3=0}, \quad (44)$$

where C_p is the specific heat at constant pressure and Q is the net surface heat flux.

In simulation 1, initially the surface heat flux is randomly imposed as $Q = -\gamma 60$ W m^{-2}, where γ is a spatially random number between 0 and 1. This heat flux is linearly decreased to 0 within the

first 2 min of the simulation. In simulation 2, the surface heat flux is randomly imposed as $Q = -\gamma 5$ W m^{-2} for the first 2 min of the computation. After the first 2 min, the surface heat is left constant as $Q = -5$ W m^{-2}. Note that these non-zeros, de-stabilizing surface heat fluxes are chosen simply to help trigger motions and thus facilitate the transition of the flow from rest towards a turbulent state. All of the parameters and conditions characterizing simulation 2 are the same as those in the simulation of McWilliams et al. (1997).

At the bottom of our domain we prescribe a Rayleigh damping layer (see Fig. 1c) in order to attenuate incoming waves (Durran, 1999), thereby preventing them from reflecting back into the domain. The thickness of the damping layer is denoted as L_d, thus the layer spans the region $0 \leqslant x_3 \leqslant L_d$. This layer is implemented by adding the following terms to the right-hand side of the momentum equation and the temperature transport equation, respectively:

$$-R_d[\bar u_i - \langle\bar u_i\rangle_{x_1x_2}], \quad (45)$$

$$-R_d[\bar\theta - \langle\bar\theta\rangle_{x_1x_2}], \quad (46)$$

where

$$R_d(x_3) = 0 \quad \text{if} \quad x_3 > L_d = \alpha_R(1 - \cos[\pi(L_d - x_3)])/2 \quad \text{if} \quad x_3 \leqslant L_d, \quad (47)$$
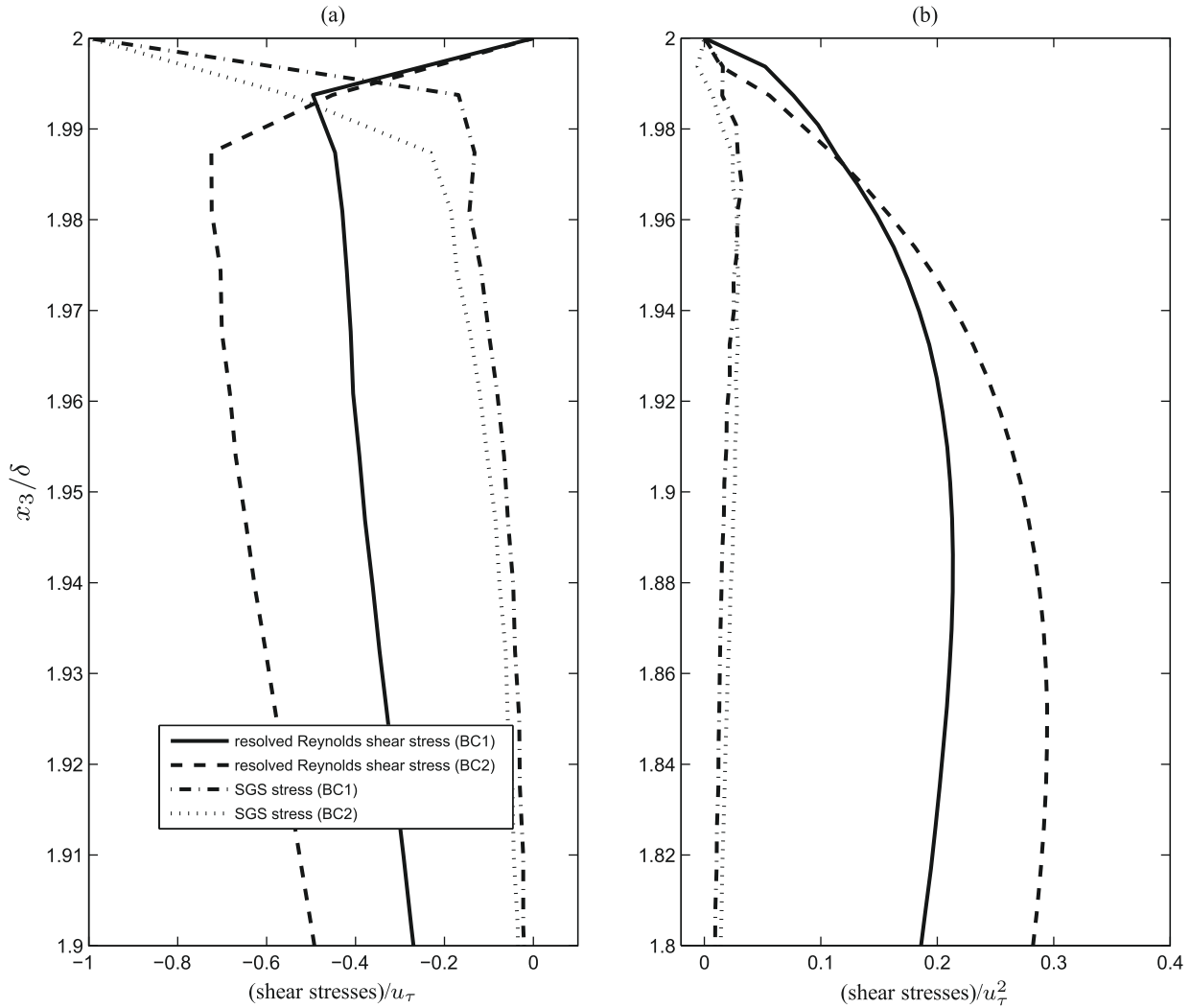
Fig. 10. Near-surface (a) downwind-vertical Reynolds and SGS shear stresses and (b) crosswind-vertical Reynolds and SGS shear stresses in an unstratified Ekman layer. Time averaging was performed over $M = 5$ periods of inertial oscillation.

and α_R^{-1} is the e-folding time scale of damping at $x_3 = 0$. In our LES the Rayleigh damping layer occupies the lower third of the water column.

Early results of simulation 1 were encouraging given that resolved horizontal features were characteristic of Langmuir cells in terms of downwind (x_1) velocity fluctuations (Fig. 14). That is, x_1-velocity fluctuations were characterized by downwind elongated streaks alternating in sign in the crosswind (x_2) direction. As seen in Fig. 14, the crosswind length scale of the Langmuir cells prior to turbulence transition is precisely the grid cell size in the crosswind direction. Initially, the grid-scale LCs are supported by the discretization. However, after transition to turbulence begins, LC nonlinear interaction generates scales (modes) beyond the support of the discretization, leading to unbounded increase of resolved turbulent kinetic energy (Fig. 11, bottom panel). This behavior is consistent with the experience of SD95 who noted that "the scale of the most unstable Langmuir circulations is much smaller than the model grid spacing".

The current discretization possesses relatively small numerical energy dissipation and is not able to attenuate the high wavenumber modes produced by LC nonlinear interaction (i.e. LC subgrid-scales). In the LES of SD95, the initial size of the cells is on the order 5–6 times the grid cell size; this size is attributed to the implicit filtering or attenuation produced by uncharacterized numerical

diffusivity. The role of the SGS parameterization is to extract energy from the smallest resolved scales (i.e. the grid-scales). In our case, the SGS model is clearly not equipped to handle the high wavenumber LC modes suggesting that new SGS parameterizations should be developed which take into account the presence of the C–L vortex force and LC subgrid-scales.

To remedy the unstable LC modes triggered by the C–L force in the stratified Ekman layer, we resort to filtering this force with a fourth-order filter at each time step, in the absence of a proper LC subgrid-scale parameterization. That is

$$\text{the filtered term} = \text{the unfiltered term} + O(h^4), \tag{48}$$

thereby adhering to the overall spatial accuracy of the method. In the horizontal directions the C–L force term is filtered with the filter defined by

$$\tilde{f} = f_i - \gamma_f(f_{i+2} - 4f_{i+1} + 6f_i - 4f_{i-1} + f_{i-2}), \tag{49}$$

where $\tilde{f}_i$ is the filtered function and f_i is the unfiltered function. Coefficient γ_f represents the strength of the filter. Parameter γ_f is taken as 1/16 following Slinn and Riley (1998). In the vertical direction, the C–L force is filtered with the fourth-order filter (adjusted for grid-stretching) discussed in Appendix.

(a)

(b)
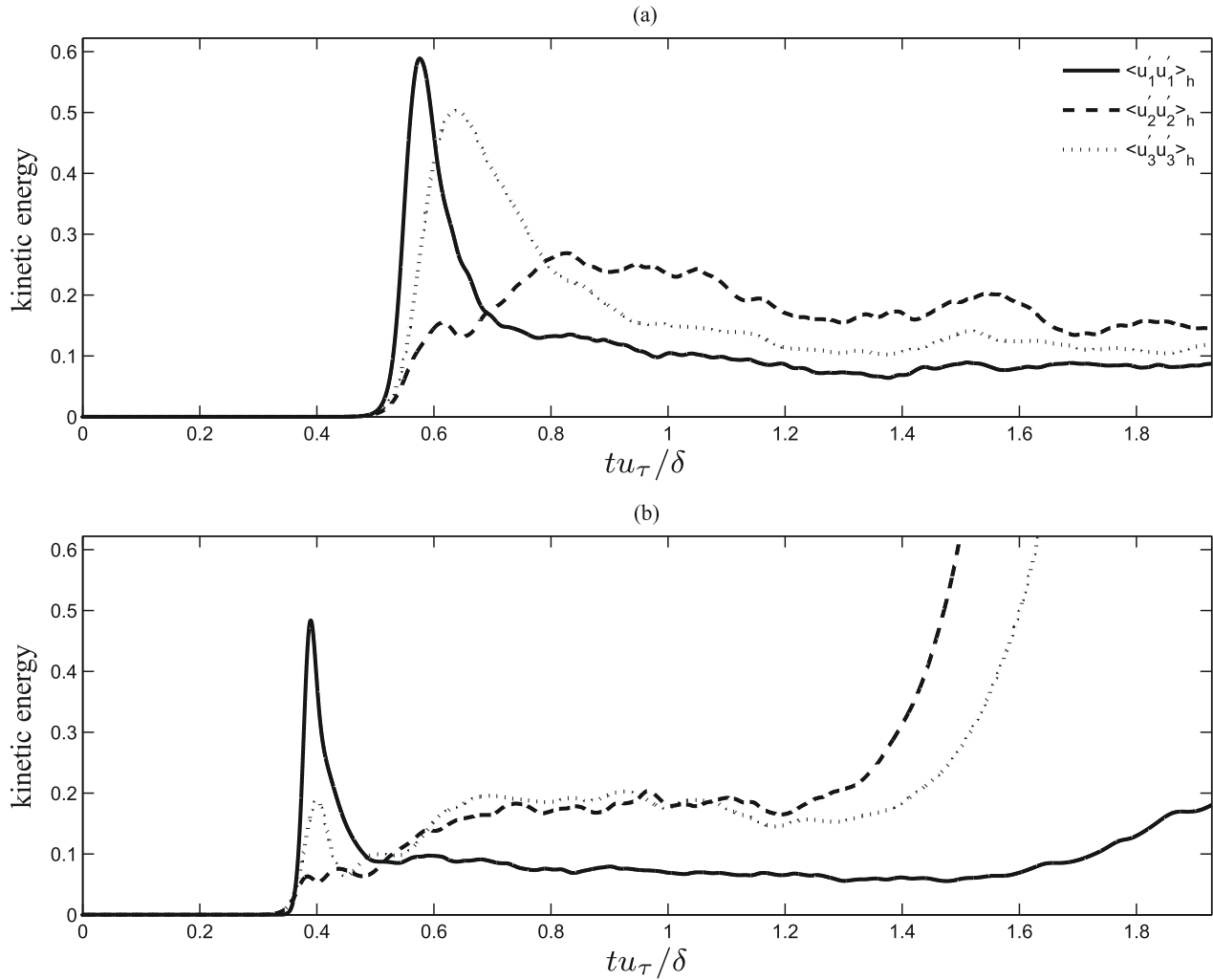
Fig. 11. Time history of turbulent kinetic energy components at $x_3/\delta = 1.886$ in a stratified Ekman layer (simulation 1) (a) with and (b) without explicit filtering of the vortex force. Surface is at $x_3/\delta = 2$.

The effectiveness of filtering the C–L force term can be seen in Fig. 11(top) as velocity fluctuations do not grow unbounded and do approach a statistically steady state after transition from rest. Additionally, we observe that the characteristic horizontal size of the initial Langmuir cells is about two times larger in the simulation with the filtered C–L force (Fig. 15) than in the simulation with the unfiltered force (Fig. 14). Ultimately, the coherence of the initial cells breaks down as a Langmuir turbulent state is reached (see Figs. 15–17). Once the cells reach the base of the mixed layer, they interact with the thermocline leading to internal wave activity. Recently Polton et al. (2008) analyzed in detail the resulting internal wave field in our simulations and found that high-frequency internal waves drain energy and momentum from the UOML over decay timescales comparable to the inertial oscillation.

Our results indicate that we may control the smallest Langmuir scales resolved in the computation via explicit filtering of the C–L force. This is a desirable attribute given that the unfiltered force leads to Langmuir scales of the same size as the grid. Scales of this size are greatly susceptible to aliasing and truncation errors and thus are poorly resolved. In traditional turbulent flows, small scales on the order of the grid size are not very energetic, thus their poor resolution does not greatly jeopardize the resolved large scales. However, this is not the case in Langmuir turbulence, as untreated (unfiltered) nonlinear interaction between Langmuir small scales serves to produce scales (modes) beyond the support of the dis-

cretization, which can lead to numerical instability. Generally it has proven difficult to compare the growth of Langmuir cells in computations with field observations as the growth and initial size of Langmuir cells can be strongly affected by numerical diffusivity (e.g. truncation errors) (see SD95) and also aliasing. In the LES of SD95, the initial size of the Langmuir cells is on the order 5–6 times the grid cell size; according to Skyllingstad and Denbo, the exact dependence of this size on numerical diffusivity is not known. Filtering of the C–L force presents an explicit way of controlling the size of the cells, and thus may pave the way for a future study of the growth of Langmuir cells without the uncertainties and adverse effects of numerical errors.

After transition towards a statistically steady state is achieved in simulation 1 (with filtered C–L force and $La_t = 0.334$) averages required for various statistical quantities are collected. These averages are taken over five inertial periods. A similar transition is also observed in simulation 2 (with filtered C–L force and $La_t = 0.3$). Averages over five inertial periods are also collected after a statistical steady state is reached. Various statistical quantities are shown in Figs. 12 and 13. An increase in the amplitude of the surface waves leads to a decrease in La_t. In the simulation with lower La_t (simulation 2), the strength of the cells is greater, leading to a more homogeneous mean downwind velocity and stronger vertical velocity fluctuations. Recall that simulation 2 is performed with the same parameters as those in the simulation of McWilliams
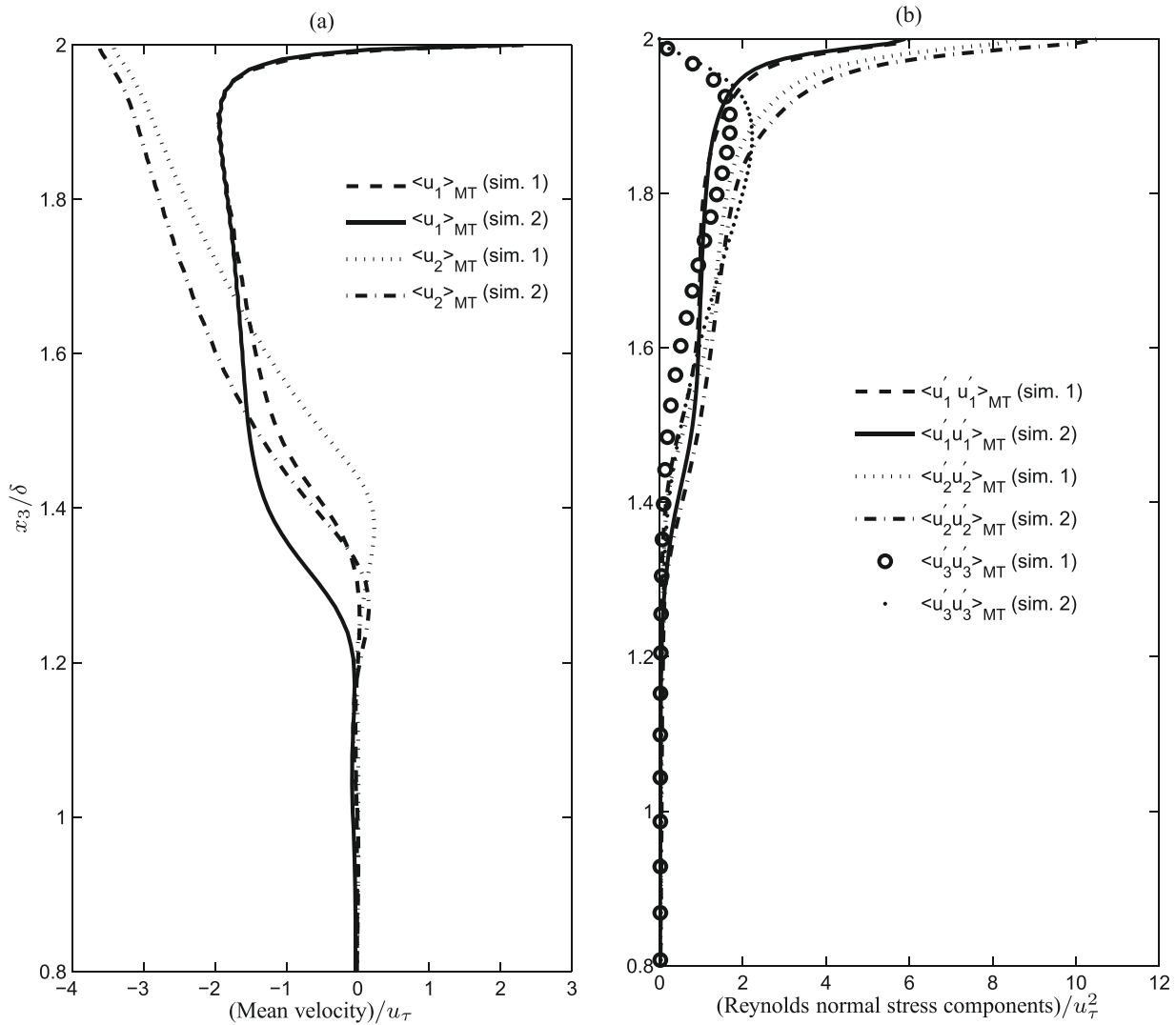
Fig. 12. (a) Mean velocity and (b) Reynolds normal stress components in a stratified Ekman layer. Time averaging was performed over $M = 5$ periods of inertial oscillation.

et al. (1997), as described earlier. Overall, the results of simulation 2 are comparable to those of McWilliams et al. (1997). Furthermore, recall that without the C–L force, the downwind bulk velocity (i.e. the net downwind transport) is zero as dictated by (41). Inclusion of the C–L force leads to

$$\int_0^{2\delta} \langle u_1 \rangle_{MT} dx_3 + \int_0^{2\delta} \frac{\phi_1^s}{La_t^2} dx_3 = 0, \tag{50}$$

thus the net downwind transport (Eulerian + Stokes drift correction) remains zero. In simulations 1 and 2, this condition is satisfied accurately, as the two terms on the left-hand side of (50) have opposite signs and are within 1% of each other in magnitude. In both simulations (1 and 2) the condition in (40) is satisfied up to within 2% error. Such a conservation condition holds for the current problem configuration given that the C–L force has zero component in the downwind direction. Finally, note the overall effect of the turbulent Langmuir number, La_t. In simulation 1, $La_t = 0.334$ while in simulation 2, $La_t = 0.3$. An increase in the amplitude of the surface waves leads to a decrease in La_t. In the simulation with lower La_t, the strength of the cells is greater, leading to a more homogeneous mean downwind velocity and stronger vertical and crosswind velocity fluctuations.

Figs. 15–19 detail the transition of the flow towards Langmuir turbulence in the simulation with filtered C–L vortex force.

Fig. 15 shows downwind velocity fluctuations on a horizontal plane near the surface and Figs. 16–19 show downwind, crosswind and vertical velocity fluctuations on a vertical plane. As can be seen from these figures, the coherence of the initial Langmuir cells breaks down as a Langmuir turbulent state is reached (Figs. 16–19). This is in contrast to the shallow water cells studied earlier, which show greater coherence during the fully developed Langmuir turbulent state. As the cells of Figs. 15–19 reach the base of the mixed layer, they interact with the thermocline generating internal wave activity (Polton et al., 2008).

The C–L vortex force is seen to trigger small scale, unstable LC in the stratified Ekman layer flow, however, this is not the case in the shallow water LSC flow described earlier in Section 4.1. The C–L vortex force is given as the cross-product between the Stokes drift velocity and flow vorticity. As described by Leibovich (1983), any crosswind anomaly in the downwind velocity produces vorticity anomalies (in the vertical direction) with opposite signs. These vorticity anomalies produce horizontal C–L vortex forces which converge in the crosswind direction over planes of local maximum downwind velocity. The converging forces give rise to the surface convergence of flow associated with the Langmuir cells.

The LES of the stratified Ekman layer starts from rest and transitions towards turbulence in response to small perturbations (on the order of the grid-scale) induced by the initially random desta-
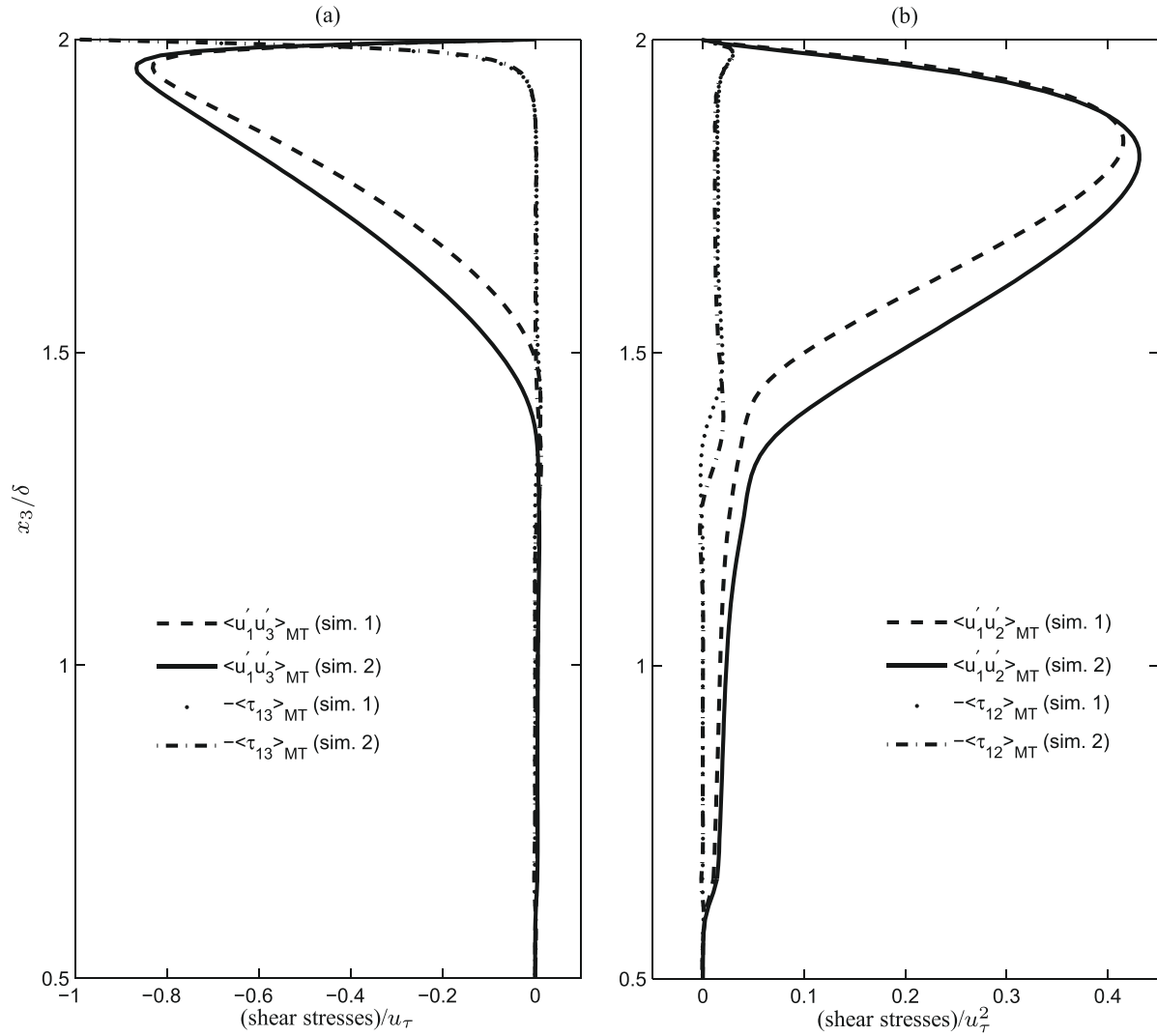
Fig. 13. (a) Downwind-vertical Reynolds and SGS shear stresses and (b) crosswind-vertical Reynolds and SGS shear stresses in a stratified Ekman layer. Time averaging was performed over $M = 5$ periods of inertial oscillation.

bilizing surface heat flux described earlier. Among these perturbations are crosswind anomalies in the downwind velocity feeding the C–L vortex force mechanism generating coherent Langmuir cells. LC nonlinear interaction leads to a loss of cell coherency and the generation of length scales beyond the support of the numerical method once transition to turbulence occurs. In contrast, LES of shallow water LSC in Section 4.1 starts from an already turbulent field containing strongly coherent Couette cells, a secondary turbulent structure characterized by crosswind anomalies of the downwind velocity over scales much larger than the grid-scale. The wavelength of these anomalies is approximately two times the depth of the water column. The C–L vortex force mechanism feeds on these large-scale Couette cells to generate the LSC described earlier which are much bigger than the grid cell size. Unlike LC in the stratified Ekman layer, the coherence of the LSC does not break down once statistically steady turbulence is reached. Note that only one Langmuir supercell is resolved in our simulation, thereby precluding nonlinear interaction between multiple supercells. Future simulations will focus on increasing the size of the domain in the horizontal directions allowing for the resolution of more supercells. It is possible that nonlinear interaction between these supercells could lead to modes beyond the support of the numerical method requiring filtering of the

C–L vortex force. Nonlinear interaction between Couette cells has been observed in the form of cell meandering by Tsukahara et al. (2006) and a similar interaction could be possible between Langmuir supercells. A detailed analysis of the Couette cells and their transition to LSC is given by Tejada-Martínez and Grosch (2007).

5. Concluding remarks

We have described a hybrid spectral/finite-difference discretization of the Navier–Stokes/Craik–Leibovich equations suitable for LES of shallow water and deep water surface mixed layer turbulent flows. Time integration is accomplished with a fractional-step scheme. The spatial and temporal accuracy of the discretization has been demonstrated for simple flows with analytical solutions and for benchmark turbulent flows.

Additional simulations with the method focused on LES-NWR of shallow water flow with full-depth LSC and on LES-NWM of an unstratified Ekman layer flow without wave effects and a stratified Ekman layer flow with wave effects (i.e. with LC). The behavior of the dynamic Smagorinsky SGS stress model was highlighted in LES-NWR of LSC and in LES-NWM of an unstratified Ekman layer flow. In the LES-NWM, the SGS stress is required to match the wind
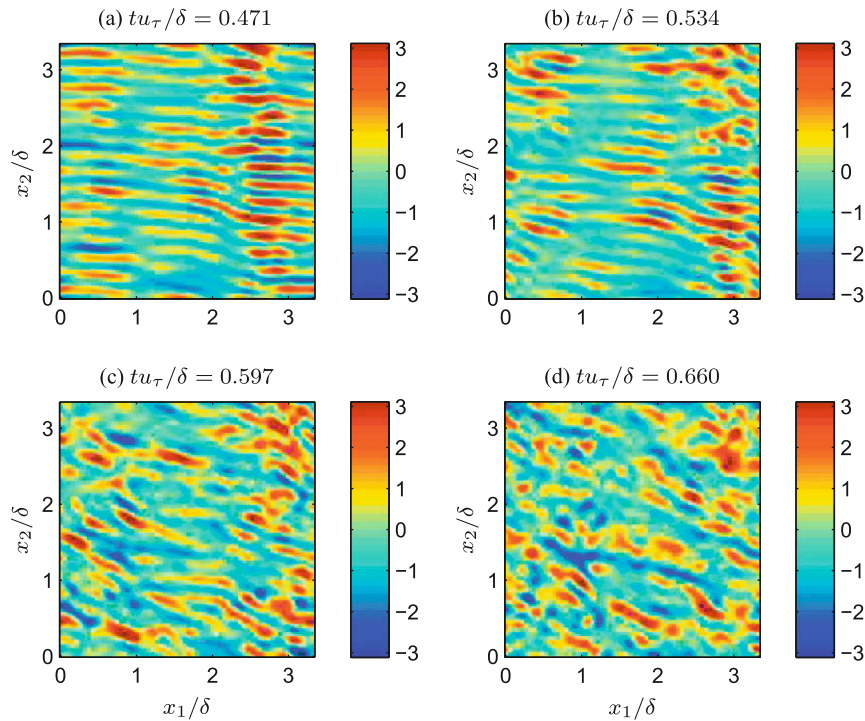
Fig. 14. Instantaneous downwind velocity fluctuation, u'_1/u_τ on horizontal plane at $x_3/\delta = 1.85$ in a stratified Ekman layer (simulation 1) without explicit filtering of the vortex force. Surface is at $x_3/\delta = 2$.
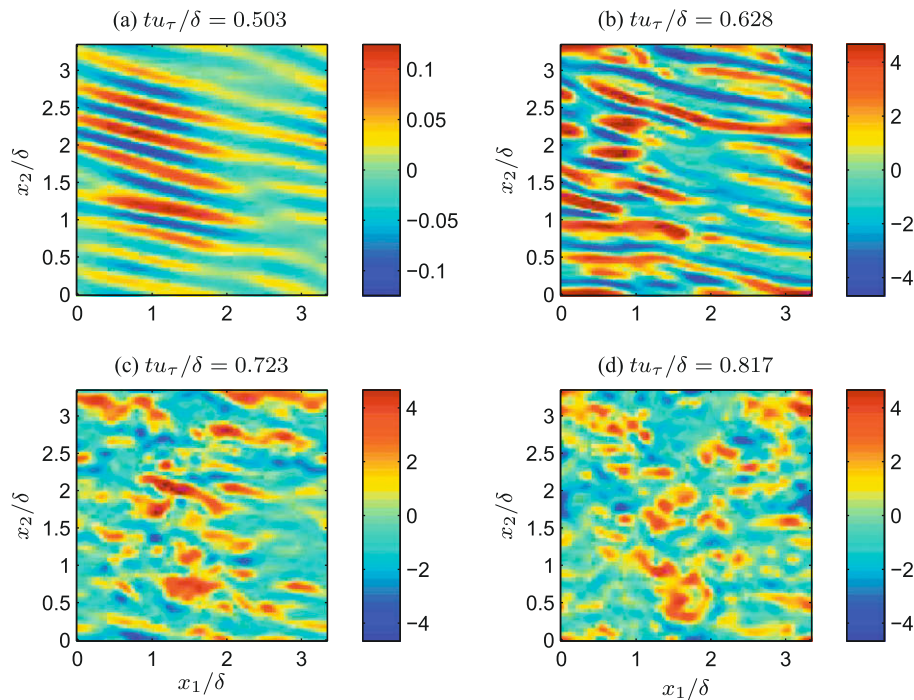
Fig. 15. Instantaneous downwind velocity fluctuation, u'_1/u_τ on horizontal plane at $x_3/\delta = 1.85$ in a stratified Ekman layer (simulation 1) with explicit filtering of the vortex force. Surface is at $x_3/\delta = 2$.

stress at the surface in the absence of a viscous stress, while in the LES-NWR, the SGS stress is not constrained to satisfy a boundary condition and thus freely tends to zero at the surface. The dominant contribution of the near-surface SGS stress in LES-NWM leads to results heavily dependent on the SGS stress parameterization. Given that LES-NWM does not resolve the surface inner layer and only resolves up to the log-layer, the SGS stress is expected to adhere to log-layer similarity theory. This similarity theory is explicitly built in the SMM. In the case of DSM, similarity is accounted for through the SGS stress boundary condition, enforcing a constant stress behavior characteristic of the log-layer. In the log-layer region, the shear stress is nearly constant and equal to the surface stress (Pope, 2000). In traditional, non-staggered grid implementations of the DSM, this constant stress condition is
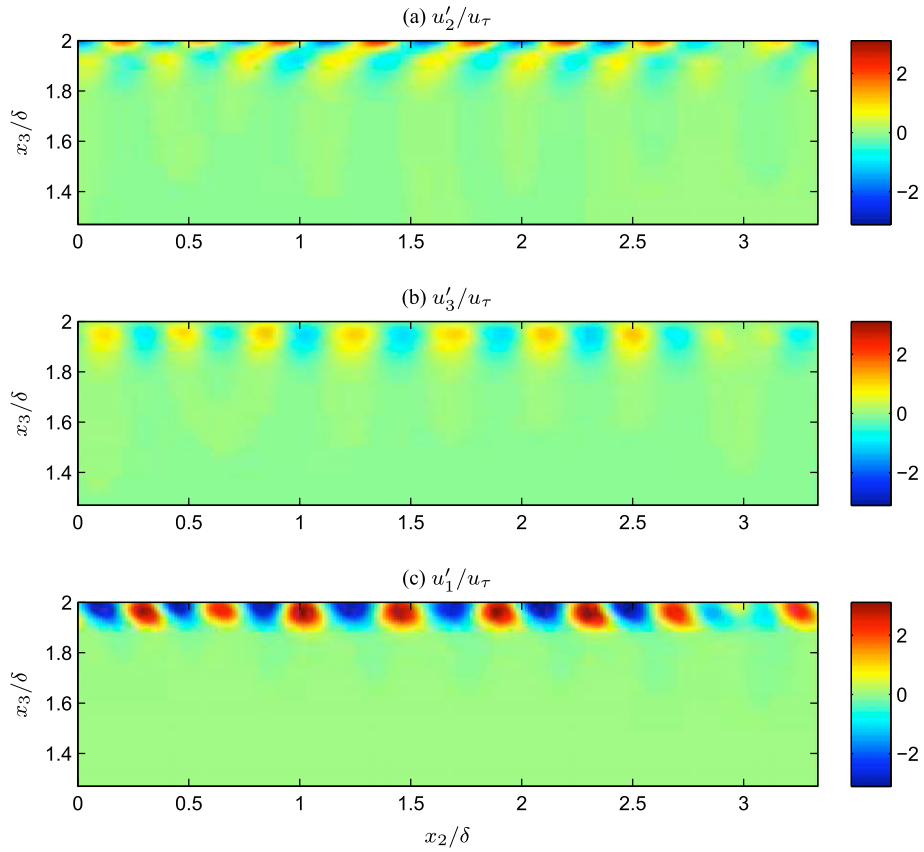
Fig. 16. Instantaneous velocity fluctuations on vertical plane at $x_1/\delta = 10/6$ and $tu_\tau/\delta = 0.503$ (simulation 1) with explicit filtering of the vortex force.
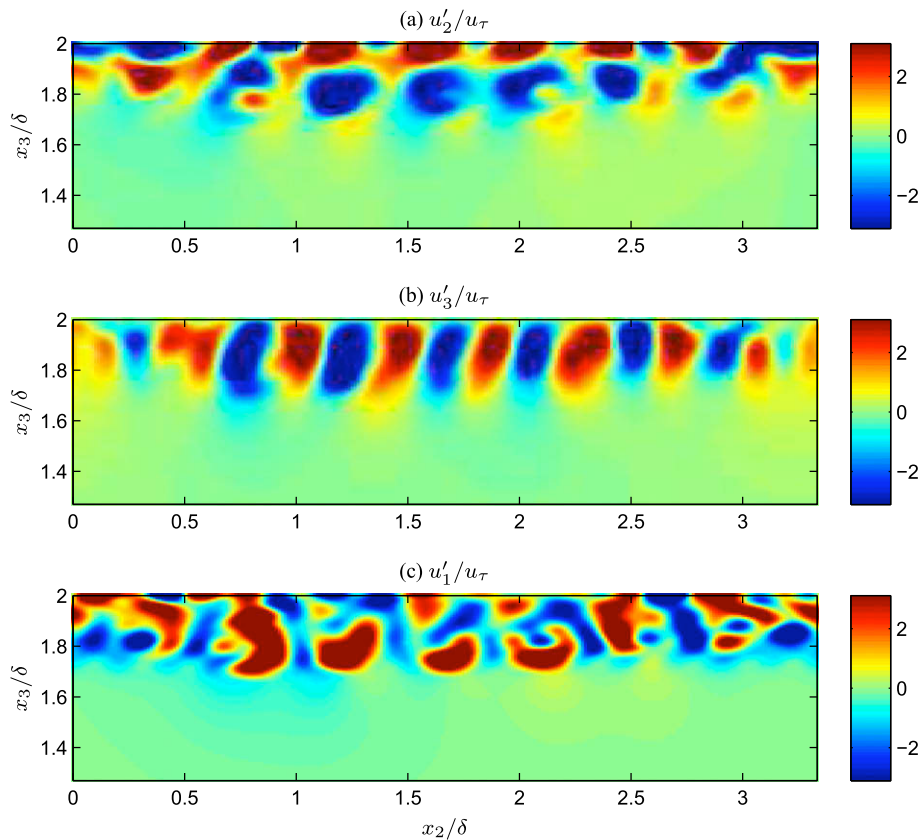
Fig. 17. Instantaneous velocity fluctuations on vertical plane at $x_1/\delta = 10/6$ and $tu_\tau/\delta = 0.628$ (simulation 1) with explicit filtering of the vortex force.
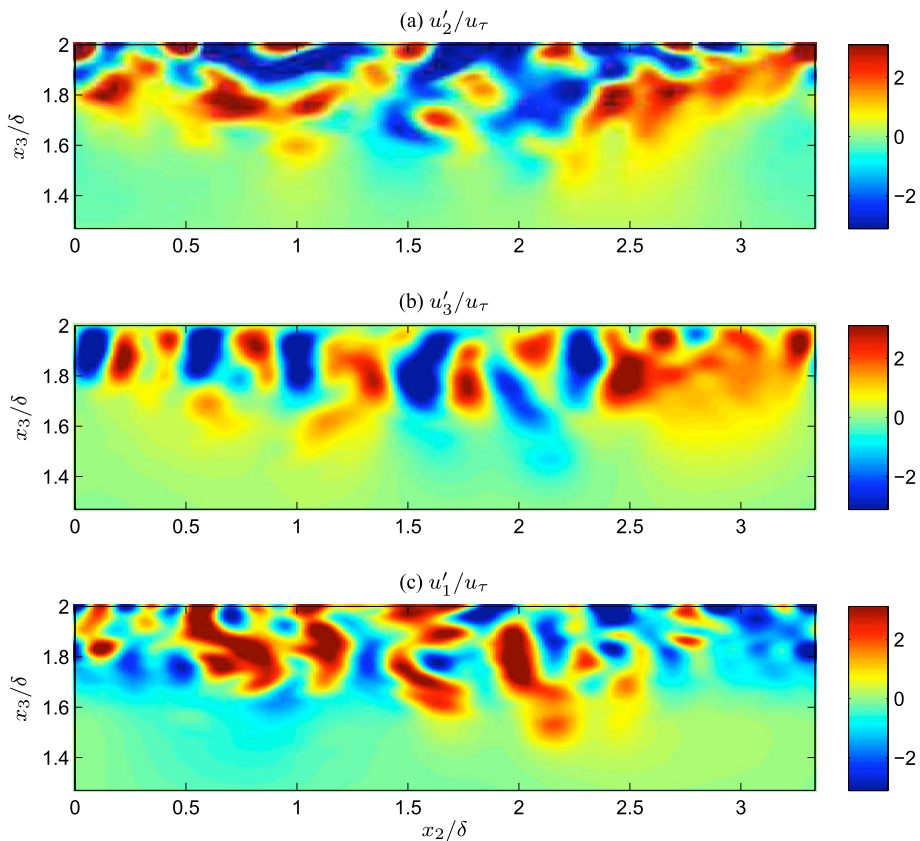
Fig. 18. Instantaneous velocity fluctuations on vertical plane at $x_1/\delta = 10/6$ and $tu_\tau/\delta = 0.723$ (simulation 1) with explicit filtering of the vortex force.
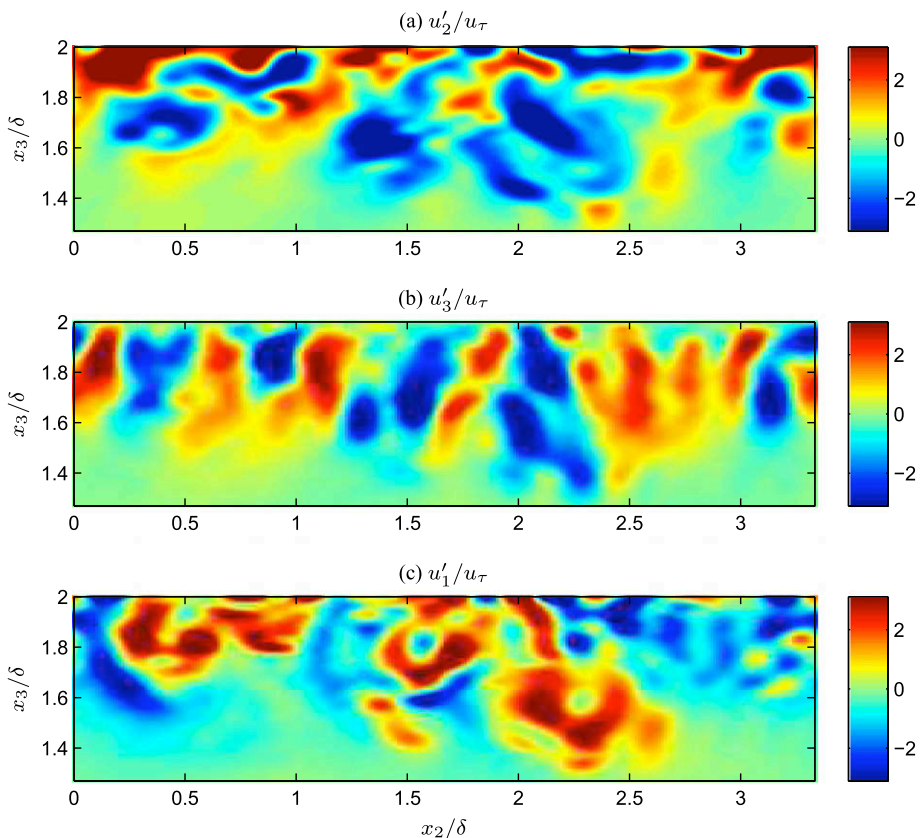
Fig. 19. Instantaneous velocity fluctuations on vertical plane at $x_1/\delta = 10/6$ and $tu_\tau/\delta = 0.848$ (simulation 1) with explicit filtering of the vortex force.

automatically satisfied as the SGS stress boundary condition is not enforced at the surface but rather at a distance half the local vertical grid cell size below the surface assumed to be within the log-layer. In our non-staggered grid formulation, this condition has to be explicitly enforced by setting the SGS stress plus the resolved Reynolds stress equal to the surface stress at the top of the domain and at the first plane of grid points below. The absence of this constant stress layer results in small SGS stress values jeopardizing the accuracy of the method.

Finally, it was seen that the C–L vortex force can trigger unstable small-scale LC. Filtering of this force suppresses the instability leading to a stable computation. We interpret this filtering operation as an ad hoc SGS model accounting for LC subgrid-scales as neither the SMM nor the DSM is able to represent these scales. As described in earlier sections, the DSM samples the smallest resolved scales in order to dynamically compute the model coefficient. In the absence of the C–L vortex force filtering operation, the rising unstable LC scales would pollute the DSM coefficient, exacerbating the instability. Our results demonstrate the need for SGS models able to account for the subgrid-scales generated by the C–L vortex force term and thus LC.

Appendix A. Validation studies

A.1. Convergence results: Taylor–Green vortices and Poiseuille laminar channel flow

Temporal and spatial convergence results are presented in terms of two canonical problems, Taylor–Green vortices and Poiseuille laminar flow, respectively. The exact solution for the two-dimensional Taylor–Green vortices problem is

$$
\begin{aligned}
u_1(t, x_1, x_2, x_3) &= -\cos(x_1)\sin(x_3)\exp(-2\nu t), \\
u_2(t, x_1, x_2, x_3) &= 0, \\
u_3(t, x_1, x_2, x_3) &= \sin(x_1)\cos(x_3)\exp(-2\nu t), \\
p(t, x_1, x_2, x_3) &= \frac{1}{4}(\cos(2x_1) + \cos(2x_3))\exp(-4\nu t),
\end{aligned}
\tag{51}
$$

for $x_i \in [0, 2\pi]$. Periodicity is taken in x_1, x_2, and x_3 and the initial condition is prescribed as (51) with $t = 0$. A second version of this problem was also tested in a domain defined by $x_1 \in [0, 2\pi]$, $x_2 \in$ $[0, 2\pi]$ and $x_3 \in [0, \pi]$ in which periodicity is taken in x_1 and x_2 and Dirichlet boundaries are taken at $x_3 = 0$ and $x_3 = \pi$. Fig. 20a clearly shows second-order temporal convergence results for the latter problem on a $33 \times 9 \times 17$ grid. Other grids were tested leading to the same temporal convergence. Although these problems are relatively simple, they can quickly lead to the discovery of coding errors. Furthermore, through these problems we have confirmed the results of Armfield and Street (2000). That is, excluding the pressure gradient from the momentum-solve in (26) or (20) leads to a first-order time-accurate method while retaining the pressure gradient leads to a second-order time-accurate method.

Fig. 20b shows spatial convergence results for a laminar Poiseuille channel flow. The exact solution is

$$
\begin{aligned}
u_1(t, x_1, x_2, x_3) &= u_{max}\left(1 - \left(\frac{x_3}{h}\right)^2\right), \\
u_2(t, x_1, x_2, x_3) &= 0, \\
u_3(t, x_1, x_2, x_3) &= 0, \\
p(t, x_1, x_2, x_3) &= p_o - \frac{2u_{max}^2}{Re_h}\frac{x_1}{h},
\end{aligned}
\tag{52}
$$

where h is the channel half-height, $Re_h = u_{max}h/\nu$ and u_{max} is the maximum centerline velocity. Note that the exact pressure solution in (52) is linear in x_1. However, the spectral discretization in x_1 and x_2 dictates that all solution variables must be periodic in these two directions. Thus, to have a periodic pressure we must take the pressure as a constant and account for the pressure gradient as a known forcing vector (f_1, f_2, f_3) added to the right-hand side of the momentum equation where $f_1 = 2u_{max}^2/Re_h$ and $f_1 = f_2 = 0$.

The initial condition is taken as $u_1 = (u_{max}/3)[1 - (x_3/h)^2]$, $u_2 = u_3 = p = 0$. Although this initial condition is not the exact solution, it is divergence free. Furthermore, note that the exact solution to this problem is time-independent. Here the time splitting in the fractional-step scheme serves as an iterator driving the numerical solution towards the exact, steady solution.

The spatial convergence result of Fig. 20b demonstrates that the spatial discretization employed is fourth-order accurate, consistent with the fourth-order spatial filter applied to the nonlinear advection term, discussed earlier.

(a) maximum error in vertical velocity

(b) error in global kinetic energy
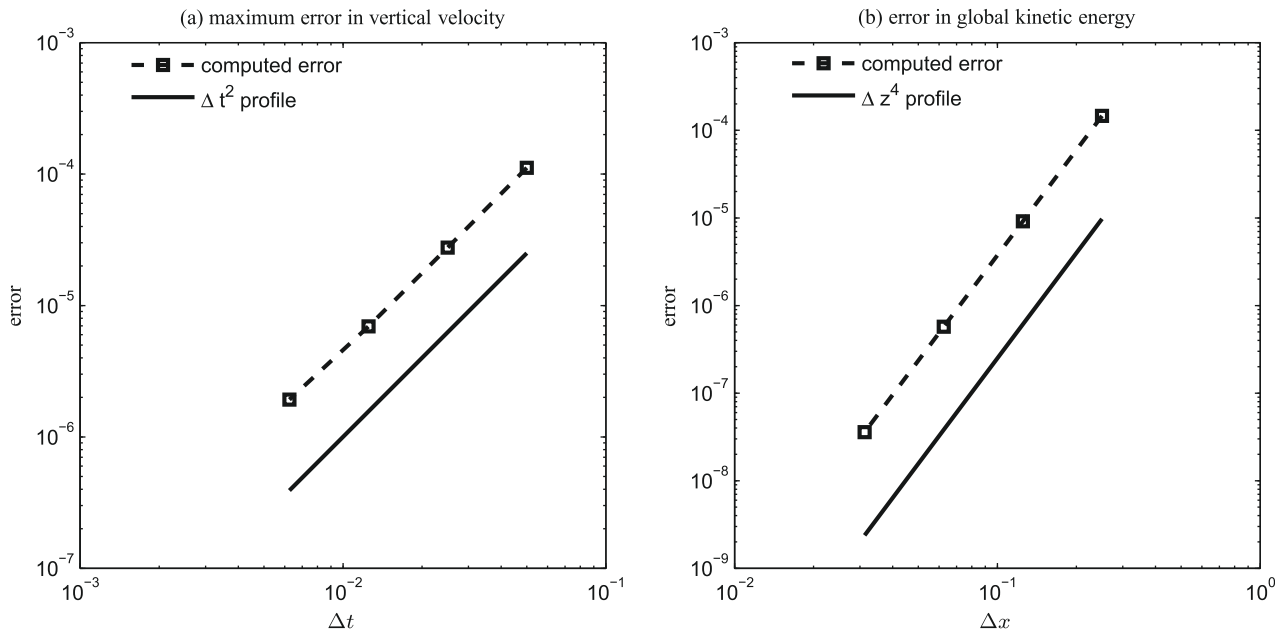
Fig. 20. (a) Temporal convergence in Taylor–Green vortices problem and (b) spatial convergence in Poiseuille channel flow problem.

A.2. Decaying isotropic turbulence

Under certain conditions, large-scale motions can become tur-
bulent. More precisely, the large-scale motions become unstable
and break into smaller scale motions which take energy from the
larger ones. Energy is passed down to such small scales at which
it is dissipated by the action of molecular viscosity. At high enough
Reynolds numbers, the small-scale motions cease to depend on the
nature of the large-scale flow, leading to the universality of small-
scale motions. Furthermore, these scales lose all directional orien-
tation, thus becoming isotropic. The energy contained within these
scales is characterized by what is usually referred to as the *five-
thirds law*. In other words, the energy at these scales behaves as
$k_r^{-5/3}$, where k_r, the radial wavenumber, is proportional the inverse
of the size of the scales. The radial wavenumber is defined as the
magnitude of wavenumber $\boldsymbol{k} = (k_1, k_2, k_3)$.

In this section we present LES results with the dynamic Smago-
rinsky model of a flow which is nearly isotropic at all scales. Our
results are compared to the experimental data of Comte-Bellot
and Corrsin (1971), who represented an infinite space of isotropic
motions decaying in time because of a lack of kinetic energy pro-
duction (in the absence of shear flow) to balance the viscous dissi-
pation. They accomplished this by obtaining a turbulent field
behind a regular grid of bars spanning a steady, uniform duct flow.
By moving at the speed of the mean flow behind the grid, they cor-
rectly surmised that an observer would see something like true
isotropic turbulence evolving in time.

Due to the homogeneity of the flow, the domain is taken as a
cube with sides of length 2π, and the boundary conditions are taken
as periodic in the x_1-, x_2- and x_3-directions. Furthermore, the cube is
represented by a grid with 33 equally spaced vertices in each direc-
tion. Thus, the uniform spacing in all directions is $h = 2\pi/32$.

Results are compared to the experimental data of Comte-Bellot
and Corrsin (1971) in the form of energy spectra, or better yet, en-
ergy contained in the different scales of the flow. The initial condi-
tion for our simulations is obtained such that its energy spectrum
matches filtered experimental spectrum at a particular non-dimen-
sional time station of the Comte-Bellot and Corrsin experiment, de-
noted as t_{42}. The simulation is run for 56 time units up to a second
non-dimensional time station, denoted as t_{98}, and the energy spec-

trum of the solution at this time is compared to the energy spec-
trum of the measured data corresponding to that same time station.

The solid curves in Fig. 21a and b show the energy spectrum of
the initial condition in our simulation matching the energy spec-
trum of the Comte-Bellot and Corrsin (1971) experiment at t_{42}.
The Reynolds number of the initial condition based on the Taylor
microscale is 71.6. The dashed curves show the energy spectrum
of the solution in our simulation at t_{98}. Fig. 21a and b show excel-
lent agreement at t_{98} between the spectrum of the experiment
(diamonds) and the spectrum of the simulation (dashed) for the
smaller resolved scales in the range $5 < k_r h < 16$. The disagree-
ment at lower wavenumbers is due to the limited length of the
sides of the cubic domain.

Fig. 21a demonstrates the effect of explicit filtering in the x_3
(vertical) direction (analogous to de-aliasing in the x_1 and x_2 (hor-
izontal) directions). Exclusion of either explicit filtering or de-alias-
ing (not shown) can lead to energy accumulation at high
wavenumbers, as shown by the dash-dotted curves in Fig. 21a.

Fig. 21b demonstrates the effect of the SGS parametrization, in
this case the dynamic Smagorinsky model. The energy spectrum in
the simulation without SGS parametrization is characterized by
excessive energy accumulation for a large part of the resolved
wavenumber range. The addition of the SGS parametrization leads
to a drastic improvement as the SGS stress serves to extract energy
from the resolved scales successfully modeling the effect of unre-
solved scales on resolved scales.

The dynamic Smagorinsky model gives $(C_s\overline{\Delta})^2$, as shown in Eq.
(10). The Smagorinsky coefficient C_s computed in our decaying iso-
tropic turbulence LES with de-aliasing and explicit vertical filtering
of the nonlinear terms for the ranges from 0.120 to 0.186, where in
Eq. (10) we have taken $\overline{\Delta} \approx h$, where $h = 2\pi/32$ is the grid size in
x_1, x_2 and x_3.

A.3. Turbulent channel flow

In this section we present DNS and dynamic Smagorinsky mod-
el LES results of an unstratified turbulent channel flow between
parallel, stationary, no-slip plates. The channel flow is chosen to
have a Reynolds number, Re_τ (based on the friction velocity, u_τ,
and the channel half-height, δ) at 180 for the purpose of compari-
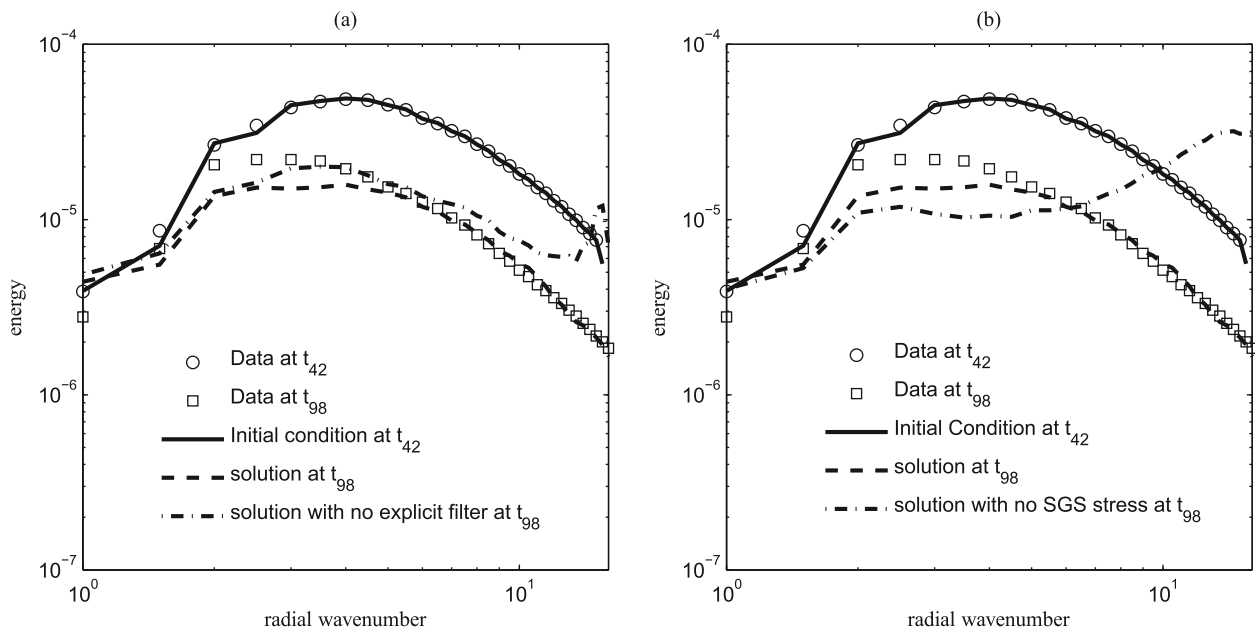
Fig. 21. (a) Effect of SGS stress model and (b) effect of explicit filtering of advection terms in the x_3 direction in decaying isotropic turbulence.

son with the benchmark DNS results of Kim et al. (1987). The interested reader is directed to Tejada-Martínez et al. (2007) for the results dealing with a stably stratified version of this flow. The friction velocity is defined as $u_\tau = (\tau_w/\rho_o)^{1/2}$, where τ_w is the shear stress at the walls. From Dean's correlation, as given by Kim et al. (1987), $Re_\tau = 180$ corresponds to a bulk Reynolds number (based on the bulk streamwise velocity and channel half-height) of 2800. The geometry of the problem is composed of no-slip walls at $x_3/\delta = \pm1$ with homogeneous spanwise (x_2) and streamwise (x_1) directions. Thus, the spanwise and streamwise directions are taken as periodic. The channel domain is taken $L_1 = 4\pi\delta$ long in the x_1 direction and $L_2 = (4/3)\pi\delta$ wide in the x_2 direction. The wall-normal direction extends from $x_3/\delta = -1$ to $x_3/\delta = 1$. The LES grid is composed of 33 points in the x_1 and x_2 directions and 65 points in the x_3 direction (i.e. $33 \times 33 \times 65$) while the DNS grid is composed of a $128 \times 128 \times 129$ grid. For our channel grid, a hyperbolic stretching function is employed in the wall-normal, x_3, direction such that the vertical distance between the first point off the top (bottom) plate and the plate itself, x_3^*, is given through $\Delta z_1^+ = 1$ for both DNS and LES. Using the stretching function, the grid spacings in the x_3 direction become smaller near the walls, yielding higher resolution in these regions. Due to the no-slip boundary conditions, a viscous boundary layer and its characteristic strong velocity gradient in the wall-normal direction develop in the near-wall region, requiring higher resolution. The first point off

the wall at $\Delta z_1^+ = 1$ is well below the top of the viscous sublayer located at $\Delta z^+ \sim 5$ (Pope, 2000). Thus our LES may be categorized as LES-NWR (i.e. LES with near-wall resolution).

In turbulent channel flow simulations, the flow is driven by a constant streamwise pressure gradient chosen such that (in a control volume setting) it balances the targeted wall shear stress determined by the choice of Re_τ. This balance results in a dimensionless streamwise pressure gradient equal to unity.

Figs. 22 and 23a and b compare root mean square (rms) of velocity fluctuations, 1–3 Reynolds stress component and mean streamwise velocity, respectively, in our DNS and LES of turbulent channel flow with the benchmark DNS of Kim et al. (1987). The rms of velocity fluctuations and the 1–3 Reynolds stress component are derived following the classical Reynolds decomposition:

$$\bar{u}_i = \langle \bar{u}_i \rangle + \bar{u}_i', \tag{53}$$

where $\langle \cdot \rangle$ denotes averaging in time and over homogeneous directions (i.e. x_1 and x_2), $\langle \bar{u}_i \rangle$ is the mean velocity and $\bar{u}_i'$ is its fluctuating component. Based on this definition, the Reynolds stress components are computed as $\langle \bar{u}_i' \bar{u}_j' \rangle = \langle \bar{u}_i \bar{u}_j \rangle - \langle \bar{u}_i \rangle \langle \bar{u}_j \rangle$ and the rms of velocity fluctuations as $u_1^{rms} = \sqrt{\langle \bar{u}_1'^2 \rangle}$, $u_2^{rms} = \sqrt{\langle \bar{u}_2'^2 \rangle}$ and $u_3^{rms} = \sqrt{\langle \bar{u}_3'^2 \rangle}$.

The agreement between the present DNS and the Kim et al. (1987) DNS in terms of rms of velocity fluctuations, 1–3 Reynolds stress component and mean streamwise velocity is remarkable gi-
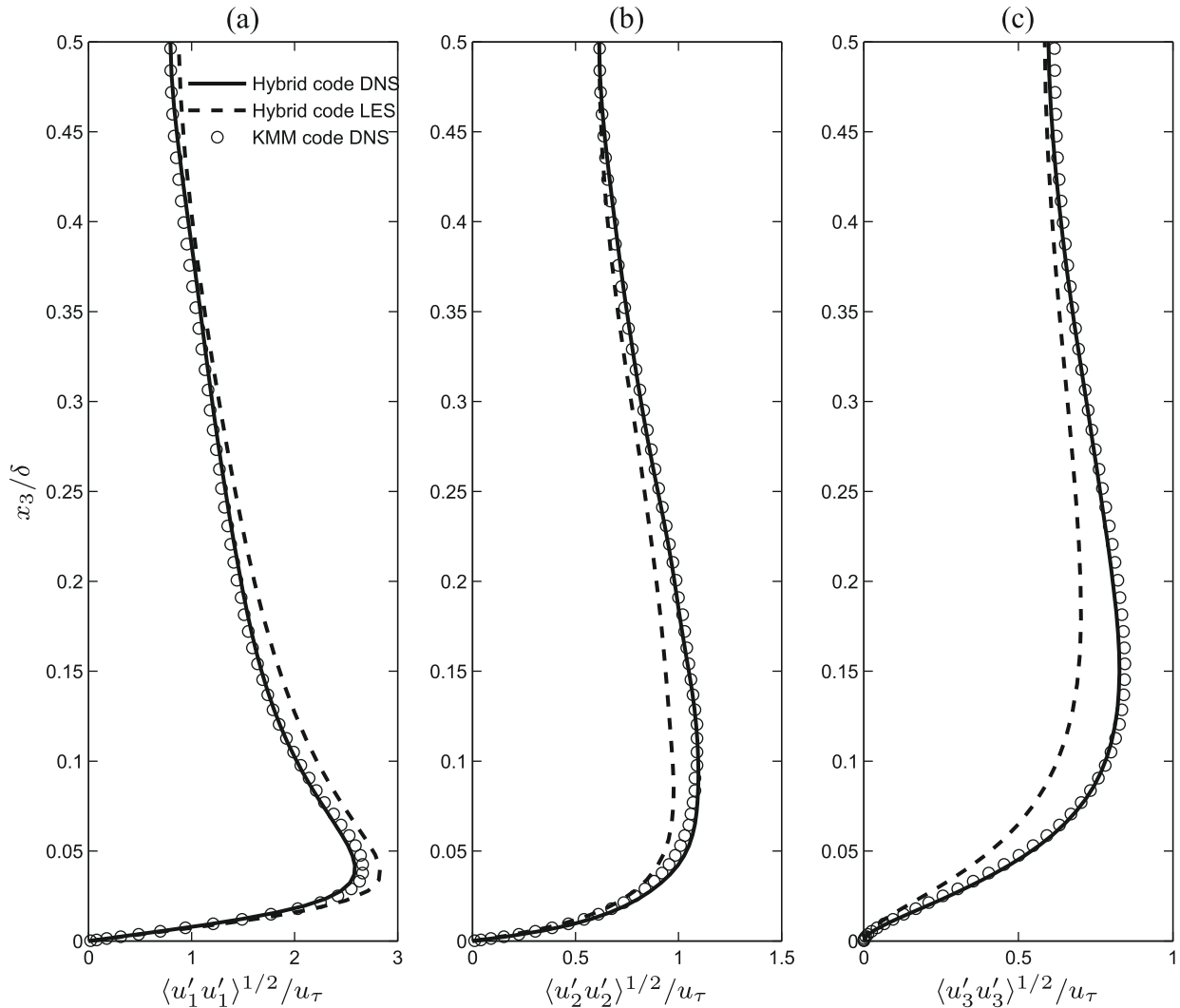
Fig. 22. Root mean square of velocity fluctuations in DNS and LES of turbulent channel flow.

(a) shear stresses
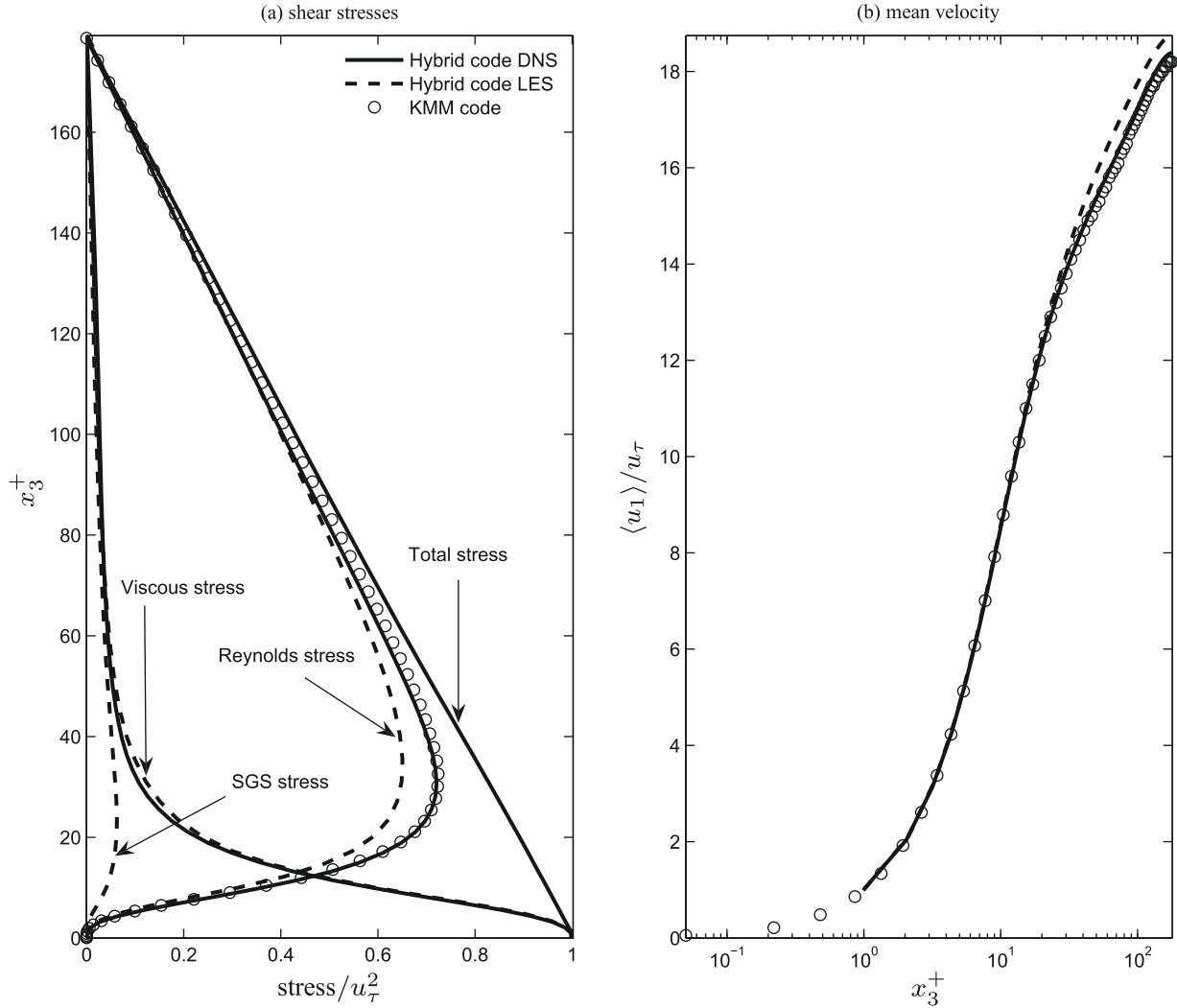
(b) mean velocity

Fig. 23. (a) Reynolds, viscous, SGS and total (Reynolds plus viscous plus SGS) shear stresses and (b) mean velocity in wall units in DNS and LES of turbulent channel flow. In DNS, the SGS stress is zero. Note that $x_3^+ = (x_3/\delta + 1)Re_\tau$.

ven that our DNS was performed on a $128 \times 128 \times 129$ grid while the DNS of Kim et al. (1987) was performed on a finer $(192 \times 160 \times 129)$ grid. Their domain was similar to ours, except in the x_2-direction, in which ours is $4\pi\delta/3$ wide while theirs is $2\pi\delta$ wide. Fig. 23a also shows the 1–3 components of the viscous stress and the Reynolds stress in the DNS and LES and the SGS stress in the LES. The sum of the 1–3 viscous and Reynolds stress components results in a straight line as expected (Pope, 2000).

Figs. 24–26 show LES results in terms of the model coefficient $(C_s\overline{\Delta})^2$ (appearing in the dynamic Smagorinsky SGS stress parametrization) and streamwise and spanwise energy spectra, respectively. Streamwise (spanwise) energy spectra are computed by taking the Fourier transform of streamwise (spanwise) autocorrelation functions. The two-point, one-time, streamwise correlation function is defined as

$$R_{ij}^x(\Delta x_1, x_3) = \frac{\left\langle \bar{u}_i'(t,x_1,x_2,x_3)\bar{u}_j'(t,x_1+\Delta x_1,x_2,x_3)\right\rangle_{tx_2}}{\left\langle \bar{u}_i'\bar{u}_j'\right\rangle}. \tag{54}$$

Similarly, the spanwise correlation function is

$$R_{ij}^y(\Delta x_2, x_3) = \frac{\left\langle \bar{u}_i'(t,x_1,x_2,x_3)\bar{u}_j'(t,x_1,x_2+\Delta x_2,x_3)\right\rangle_{tx_1}}{\left\langle \bar{u}_i'\bar{u}_j'\right\rangle}, \tag{55}$$

where $\langle\cdot\rangle_{tx_i}$ denotes averaging in time and over the x_i-direction. Autocorrelations are obtained by setting $i = j$ in (54) and (55) and ignoring the usual convention of summing over repeated indices.

Near the wall, $(C_s\overline{\Delta})^2$ goes to zero as can be seen by analyzing Eqs. (10)–(12). As expected, near the wall $(C_s\overline{\Delta})^2 \sim z^{+3} = (Re_\tau z)^3$ where z is the dimensionless distance to the wall (Pope, 2000). Streamwise and spanwise energy spectra at the middle horizontal plane and a near-wall horizontal plane of the channel from our LES compared to those from the DNS of Kim et al. (1987) demonstrates that the LES is able to accurately represent the energy in the most energetic scales of the flow. As expected, there is small damping of energy in the LES relative to the DNS at the highest resolved wavenumbers of the LES. This damping is due to an unknown combination of the spatiotemporal discretization and the SGS parameterization. Note that the high wavenumber energy damping observed in LES with our high-order spatial discretization is much less that the damping observed in LES with lower order methods. For comparison, the reader is directed to the LES results of Najjar and Tafti (1996) obtained with a second-order accurate spatial discretization. In the latter, excessive streamwise energy damping occurs at $k_1 h \sim 10$. Finally, the reader is reminded that it is not possible to compare our LES energy spectra at the
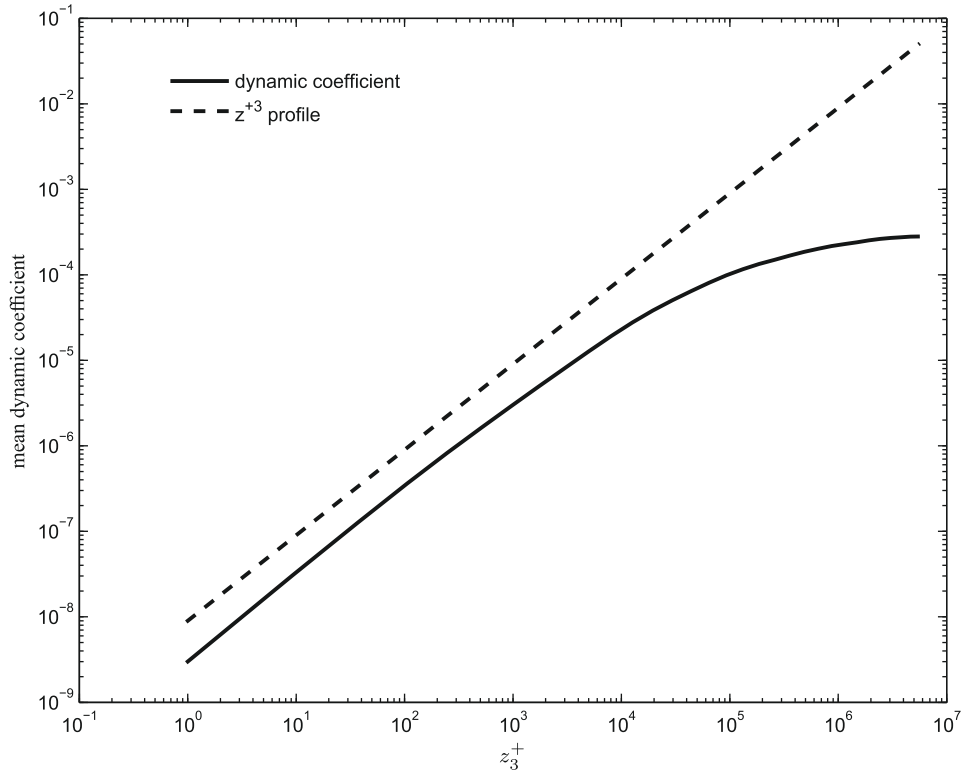
Fig. 24. Mean dynamic coefficient, $\langle C_s^2 \Delta^2 \rangle$, in LES of turbulent channel flow.
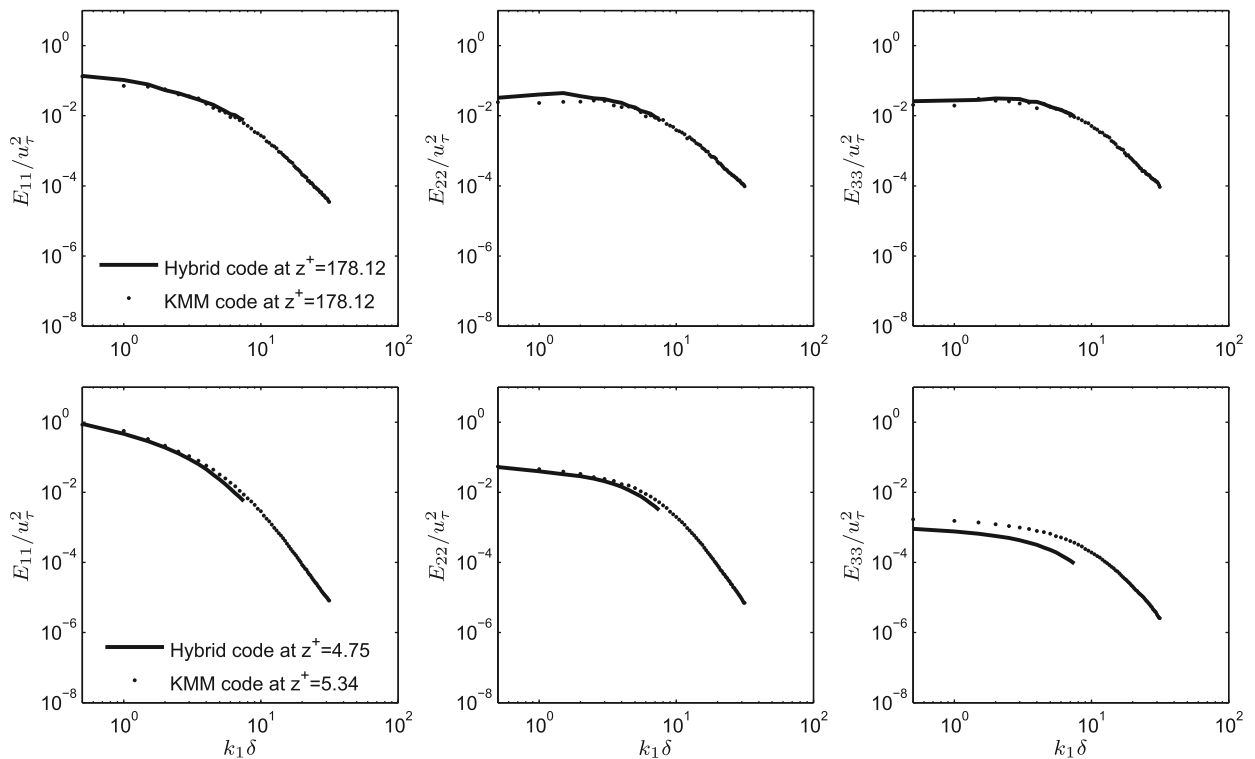
Fig. 25. Streamwise one-dimensional energy spectra in LES of turbulent channel flow.

same near-wall locations as those of Kim et al. (1987) due to different grids between our LES and their DNS. As a result, LES energy spectra in terms of wall-normal fluctuations at $z^+ = 4.75$ are lower than the DNS counterpart at $z^+ = 5.34$ for all wavenumbers resolved in the LES.

Appendix B. Finite-difference stencils

Most of the description of the finite-difference stencils appears in Tejada-Martínez and Grosch (2007). We present it here for completeness.
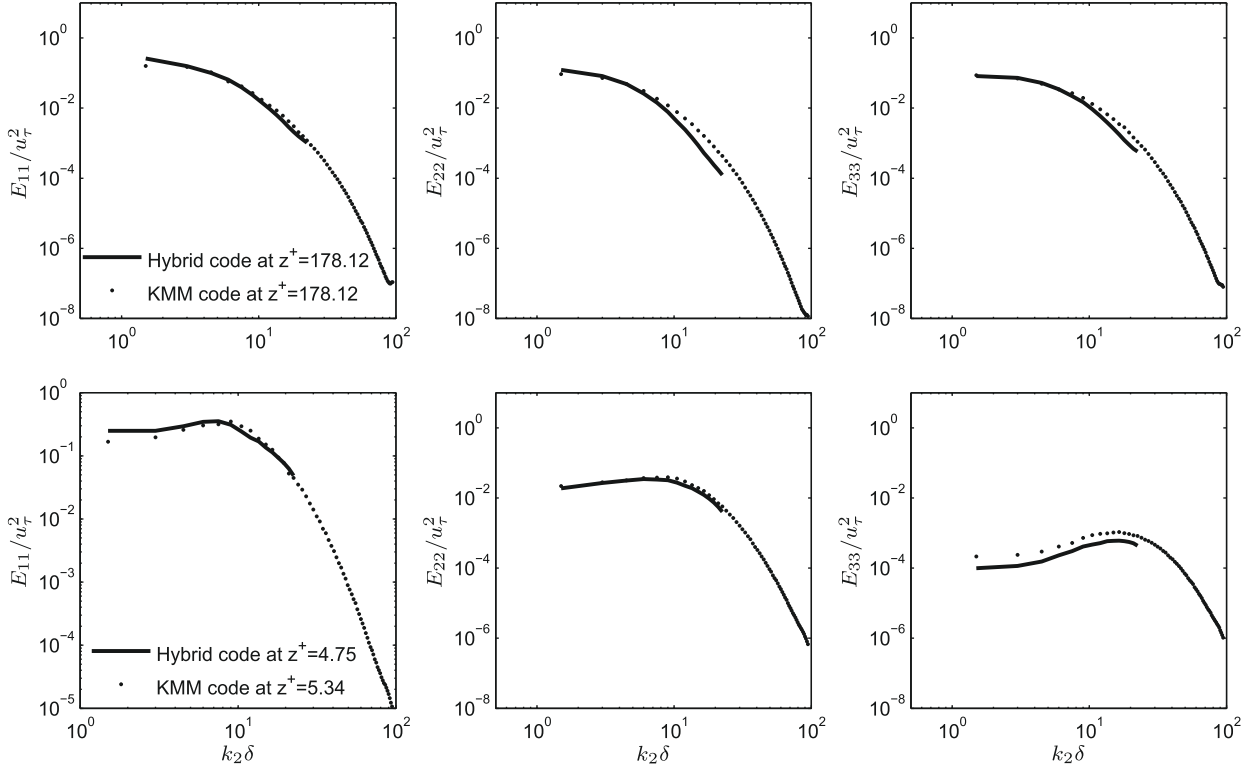
Fig. 26. Spanwise one-dimensional energy spectra in LES of turbulent channel flow.

In order to resolve strong gradients in the x_3-direction near the bottom boundary and the top surface, a greater number of points is clustered near these two regions. Consider a set of equi-distant points at locations ξ_i discretizing the vertical direction of the domain. Clustering or stretching of these points may be accomplished through a mapping hyperbolic function (with existing real inverse) such as

$$z_i = (1/b) \; \tanh[\xi_i \tanh^{-1}(b)]. \tag{56}$$

This function takes the set of N equi-distant points ξ_i discretizing the interval $[-1, 1]$ and maps them to the set of N non-uniformly spaced points z_i in $[-1, 1]$. In our LES-NWR of shallow water Langmuir circulation, the points z_i are clustered near the upper and lower bounds of the interval. In our LES-NWM of stratified and unstratified Ekman layers, the points are clustered near the surface only. Coefficient b is a measure of the clustering.

The finite-difference approximations of $\partial/\partial x_3$ and $\partial^2/\partial x_3^2$ used here (i.e. $\delta/\delta x_3$ and $\delta^2/\delta x_3^2$, see further ahead) can only be applied over points which are equi-distant. Thus, derivatives on the non-uniform grid are computed in terms of derivatives on the equi-distant grid and derivatives of the inverse of the mapping function as

$$\frac{df}{dz} = \frac{df}{d\xi}\frac{d\xi}{dz} \quad \text{and} \quad \frac{d^2f}{dz^2} = \frac{d^2f}{d\xi^2}\left(\frac{d\xi}{dz}\right)^2 + \frac{df}{d\xi}\frac{d^2\xi}{dz^2}, \tag{57}$$

where z and ξ denote z_i and ξ_i, respectively, in (56). Note that this approach to clustering leads to non-uniformly spaced grid points in the vertical direction only. The grid points are uniformly spaced in the horizontal directions.

Using compact finite-difference schemes, second- and first-order derivatives of function $f(\xi)$ on $[a, b]$ are obtained. Consider the set $\{\xi_1, \xi_2, \xi_3, \ldots, \xi_N, \xi_{N+1}\}$ of equi-distant points gridding the interval $[a, b]$ with h being the distance between the points. The second and first derivatives of $f(\xi)$ may be obtained from

$$\boldsymbol{A}\boldsymbol{f}'' = \boldsymbol{B}\boldsymbol{f} \quad \text{thus} \quad \boldsymbol{f}'' = \left\{\boldsymbol{A}^{-1}\boldsymbol{B}\right\}\boldsymbol{f}, \tag{58}$$

and

$$\boldsymbol{C}\boldsymbol{f}' = \boldsymbol{D}\boldsymbol{f} \quad \text{thus} \quad \boldsymbol{f}' = \left\{\boldsymbol{C}^{-1}\boldsymbol{D}\right\}\boldsymbol{f}, \tag{59}$$

where $\boldsymbol{f} = (f_1, f_2, \cdots, f_N)^t$ and f_i is $f(z)$ evaluated at $z_i \in [a, b]$. Matrices $\boldsymbol{A}$, $\boldsymbol{B}$, $\boldsymbol{C}$ and $\boldsymbol{D}$ are banded. However, matrices $\boldsymbol{A}^{-1}\boldsymbol{B}$ and $\boldsymbol{C}^{-1}\boldsymbol{D}$ are full. Next, the stencils used to generate these matrices are detailed.

B.1. First-order derivative

Let f_i' denote the first derivative of $f(z)$ at $z = z_i$. For $i > 2$ and $i < N$, the first derivative of function $f(z)$ is approximated via

$$\frac{1}{3}f_{i-1}' + f_i' + \frac{1}{3}f_{i+1}' = \frac{1}{h}\left(-\frac{1}{36}f_{i-2} - \frac{7}{9}f_{i-1} + \frac{7}{9}f_{i+1} + \frac{1}{36}f_{i+2}\right). \tag{60}$$

Detailed analysis of this $O(h^6)$ approximation is given by Lele (1992). For $i = 1$, the first derivative may be obtained from the following $O(h^5)$ approximation:

$$f_1' = \frac{1}{h}(c_1 f_1 + c_2 f_2 + c_3 f_3 + c_4 f_4 + c_5 f_5 + c_6 f_6 + c_7 f_7 + c_8 f_8), \tag{61}$$

where

$$
\begin{aligned}
c_1 &= -(\alpha_0 - 28\beta_0 + 13,068)/5040, \\
c_2 &= +(\alpha_0 - 27\beta_0 + 5040)/720, \\
c_3 &= -(\alpha_0 - 26\beta_0 + 2520)/240, \\
c_4 &= +(\alpha_0 - 25\beta_0 + 1680)/144, \\
c_5 &= -(\alpha_0 - 24\beta_0 + 1260)/144, \\
c_6 &= +(\alpha_0 - 23\beta_0 + 1008)/240, \\
c_7 &= -(\alpha_0 - 22\beta_0 + 840)/720, \\
c_8 &= +(\alpha_0 - 21\beta_0 + 720)/5040,
\end{aligned}
\tag{62}
$$

$\alpha_0 = 1809.257$ and $\beta_0 = -65.1944$. For $i = 2$, the first derivative may be obtained from the following $O(h^5)$ approximation:

$$f_2' = \frac{1}{h}(d_1 f_1 + d_2 f_2 + d_3 f_3 + d_4 f_4 + d_5 f_5 + d_6 f_6 + d_7 f_7 + d_8 f_8), \quad (63)$$

where

$$
\begin{aligned}
d_1 &= -(\alpha_1 - 21\beta_1 + 720)/5040, \\
d_2 &= +(\alpha_1 - 20\beta_1 - 1044)/720, \\
d_3 &= -(\alpha_1 - 19\beta_1 - 720)/240, \\
d_4 &= +(\alpha_1 - 18\beta_1 - 360)/144, \\
d_5 &= -(\alpha_1 - 17\beta_1 - 240)/144, \\
d_6 &= +(\alpha_1 - 16\beta_1 - 180)/240, \\
d_7 &= -(\alpha_1 - 15\beta_1 - 144)/720, \\
d_8 &= +(\alpha_1 - 14\beta_1 - 120)/5040,
\end{aligned}
\quad (64)
$$

$\alpha_1 = -262.16$ and $\beta_1 = -26.6742$. Similar expressions for the first derivatives are defined at $i = N$ and $i = N + 1$. The stencils in (61)–(64) are analyzed in detail by Carpenter et al. (1993).

B.2. Alternate first-order derivative

The previously described vertical derivative at $i = 1$ and $i = N + 1$ proved effective for non-zero shear stress and no-slip boundary conditions. However, in the case of the zero shear stress boundary conditions at the bottom of the domain in Ekman layer simulations, this approximation leads to undesired inaccuracies. For example, consider imposing $du_1/dx_3 = 0$ at the bottom of the domain, as is the case for the unstratified and stratified Ekman layer simulations. Following the previously described formulation,

$$\frac{du_1}{dx_3} = \frac{du_1}{d\xi}\frac{d\xi}{dx_3} = 0, \quad (65)$$

where $d\xi/dx_3$ is the vertical derivative of stretching function $\xi(x_3)$ which maps a set of stretched grid points on x_3 to a set of regularly spaced grid points on ξ. The derivative $du_1/d\xi$ in (65) mentioned above is approximated through Eq. (61) valid for a regularly spaced grid. A major deficiency of the formulation previously described is that Eq. (65) implies that

$$\frac{du_1}{d\xi} = 0. \quad (66)$$

Thus, the true zero derivative boundary condition on a stretched grid is not imposed and instead is replaced by an erroneous zero derivative on a regularly spaced grid. A more accurate approximation of the derivative was implemented at the bottom without requiring the stretching function derivative (i.e. $d\xi/dz$). A third-order accurate expression for the first derivative was implemented, derived via Taylor series expansions taking into consideration the vertical variability of the grid. The vertical derivative of a quantity f (i.e. df/dx_3) at the bottom of the domain was taken as

$$f_1' = -a_1 f_1 - a_2 f_2 - a_3 f_3, \quad (67)$$

where

$$a_1 = -1/\lambda_1, \quad a_2 = \lambda_2/\lambda_1, \quad a_3 = \lambda_3/\lambda_1, \quad (68)$$

with

$$\lambda_1 = \frac{-h_1 h_2 (h_1 + h_2)}{(h_1 + h_2)^2 - h_1^2}, \quad \lambda_2 = \frac{(h_1 + h_2)^2}{(h_1 + h_2)^2 - h_1^2},$$

$$\lambda_3 = \frac{h_1^2}{(h_1 + h_2)^2 - h_1^2}. \quad (69)$$

In the previous expression h_1 is the vertical distance between the first two grid points starting at the bottom, and so on. A similar expression for df/dx_3 at the surface was also implemented for consistency. Although the previous approximation of the first-order derivative is third-order accurate, it is well known that boundary

stencils may be one order less than interior stencils without degrading the overall spatial accuracy of the interior scheme (e.g. see Kreiss, 1972). Our interior scheme is fourth-order accurate, as was shown in the validation studies and is described further in the upcoming subsection.

B.3. Second-order derivative

For $i > 2$ and $i < N$, the second derivative of function $f(z)$ is computed using the following $O(h^6)$ approximation discussed by Lele (1992):

$$\frac{2}{11}f_{i-1}' + f_i' + \frac{2}{11}f_{i+1}' = \frac{1}{h^2}\left(\frac{3}{44}f_{i-2} + \frac{12}{11}f_{i-1} - \frac{51}{22}f_i + \frac{12}{11}f_{i+1} + \frac{3}{44}f_{i+2}\right). \quad (70)$$

For $i = 1$, the second derivative may be obtained from the following $O(h^5)$ approximation:

$$f_1'' = \frac{1}{h^2}(c_1 f_1 + c_2 f_2 + c_3 f_3 + c_4 f_4 + c_5 f_5 + c_6 f_6 + c_7 f_7 + c_8 f_8), \quad (71)$$

where $c_1 = 5.211$, $c_2 = -22.300$, $c_3 = 43.950$, $c_4 = -52.722$, $c_5 = 41.000$, $c_6 = -20.100$, $c_7 = 5.661$ and $c_8 = -0.700$. For $i = 2$, the second derivative may be obtained from the following $O(h^5)$ approximation:

$$f_2'' = \frac{1}{h^2}(d_1 f_1 + d_2 f_2 + d_3 f_3 + d_4 f_4 + d_5 f_5 + d_6 f_6 + d_7 f_7 + d_8 f_8), \quad (72)$$

where $d_1 = 0.700$, $d_2 = -0.389$, $d_3 = -2.700$, $d_4 = 4.750$, $d_5 = -3.722$, $d_6 = 1.800$, $d_7 = -0.500$ and $d_8 = 0.061$. Similar expressions for the second derivatives are defined at $i = N$ and $i = N + 1$. The stencils in (71) and (72) are courtesy of Jackson (University of Illinois at Urbana-Champaign, personal communication) and may be derived using a similar approach to that of Carpenter et al. (1993).

When solving Poisson's equation for pressure in (28), the following alternate expressions are used (instead of (71) and (72)) leading to lower round-off errors. For $i = 1$

$$
\begin{aligned}
f_1'' = &-\frac{1}{h}\frac{49}{10}f_1' \\
&+ \frac{1}{h^2}\left(\frac{13,489}{1800}f_1 + 12f_2 - \frac{15}{2}f_3 + \frac{40}{9}f_4 - \frac{15}{8}f_5 + \frac{12}{25}f_6 - \frac{1}{18}f_7\right),
\end{aligned}
\quad (73)
$$

with truncation error $0.6572 h^6 d^8 f/dz^8$. Note that the Neumann pressure boundary condition in (28) is assigned through the first term on the right-hand side of (73). For $i = 2$,

$$
\begin{aligned}
&\frac{11}{128}f_{i-1}'' + f_i'' + \frac{11}{128}f_{i+1}'' \\
&= \frac{1}{h^2}\left(\frac{585}{512}f_1 - \frac{141}{64}f_2 + \frac{459}{512}f_3 + \frac{9}{32}f_4 - \frac{85}{512}f_5 + \frac{3}{64}f_6 - \frac{3}{512}f_7\right),
\end{aligned}
\quad (74)
$$

with truncation error $0.02101 h^6 d^8 f/dz^8$. Similar expressions are used for $i = N + 1$ and $i = N$. The approximations in (73) and (74) and their corresponding truncation errors were derived via Taylor series analysis.

B.4. Spatial filtering of advection terms

As discussed earlier, the advection terms in the momentum equations are spatially filtered in the vertical direction at each time step in order to damp out scales of motion unresolvable by the grid. The following fourth-order compact filter adapted for a non-uniform grid (Slinn and Riley, 1998) is used:

$$0.4\tilde{f}_{i-1} + \tilde{f}_i + 0.4\tilde{f}_{i+1}$$

$$= 0.4f_{i-1} + f_i + 0.4f_{i+1} - \frac{1}{80}(f_{i+2} - 4f_{i+1} + 6f_i - 4f_{i-1} + f_{i-2})$$

$$- \frac{h}{80}\left(\frac{6\gamma_2(z_i)}{\gamma_1^2(z_i)}\right)\left(\frac{f_{i+2} - 2f_{i+1} + 2f_{i-1} - f_{i-2}}{2}\right)$$

$$- \frac{h^2}{80}\left(\frac{4\gamma_3(z_i)}{\gamma_1^3(z_i)} + \frac{3\gamma_2^2(z_i)}{\gamma_1^4(z_i)}\right)(f_{i+1} - 2f_i + u_{i-1})$$

$$- \frac{h^3}{80}\left(\frac{\gamma_4(z_i)}{\gamma_1^4(z_i)}\right)\left(\frac{f_{i+1} - f_{i-1}}{2}\right), \tag{75}$$

where $\gamma_1 = \partial\xi/\partial z$, $\gamma_2 = \partial^2\xi/\partial z^2$, $\gamma_3 = \partial^3\xi/\partial z^3$ and $\gamma_4 = \partial^4\xi/\partial z^4$ and ξ is a mapping function in (56). Note that this stencil is not valid for points at the bottom and top boundaries and for the first two horizontal planes of points off from these boundaries. In the current implementation the filter is not applied at these points. This omission does not have a negative impact on the results.

A formal derivation of this compact filter can be made through Taylor series analysis. From this analysis one can see that the filtered function is an approximation of the unfiltered function up to fourth-order. That is

$$\tilde{f} = f + O(h^4). \tag{76}$$

The finite-difference approximations of the first and second derivatives in the vertical (x_3) direction (discussed in the previous subsection) introduce an error of $O(h^5)$ or higher. Filtering the advection terms in the vertical direction using (75) introduces an error of $O(h^4)$. Furthermore, using a spectral discretization in the horizontal (x_1 and x_2) directions introduces an error of much higher order than the previously discussed finite differencing and filtering operations. Thus, the current spatial discretization is at least of $O(h^4)$. A higher order filter could potentially be introduced, however, this would involve a more expensive computation at the expense of only minimally changing results.

References

Armenio, V., Sarkar, S., 2002. An investigation of stably stratified turbulent channel flow using large-eddy simulation. J. Fluid Mech. 459, 1–42.

Armfield, S.W., Street, R., 2000. Fractional step methods for the Navier–Stokes equations on non-staggered grids. ANZIAM J. 42, C134–C156.

Basu, S., Porté-Agel, F., 2006. Large-eddy simulation of stably stratified atmospheric boundary layer turbulence: a scale-dependent dynamic modeling approach. J. Atmos. Sci. 63, 2074–2091.

Beare, R.J., MacVean, M.K., Holtslag, A.A.M., Cuxart, J., Esau, I., Golaz, J.C., Jimenez, M.A., Khairoutdinov, M., Kosovic, B., Lewellen, D., Lund, T.S., Lundquist, J.K., McCabe, A., Moene, A.F., Raasch, N.Y.S., Sullivan, P., 2006. An intercomparison of large-eddy simulations of the stable boundary layer. Bound. Layer Meteor. 118, 247–272.

Carpenter, M.H., Gotlieb, D., Abarbanel, S., 1993. The stability of numerical boundary treatments for compact high-order finite difference schemes. J. Comput. Phys. 108, 272–292.

Coles, D., 1956. The law of the wake in the turbulent boundary layer. J. Fluid Mech. 1, 191–226.

Comte-Bellot, G., Corrsin, S., 1971. Simple Eulerian time correlation of full and narrow-band velocity signals in grid-generated isotropic turbulence. J. Fluid Mech. 48, 273–337.

Craik, A.D.D., Leibovich, S., 1976. A rational model for Langmuir circulation. J. Fluid Mech. 73, 401–426.

Durran, D.R., 1999. Numerical Methods for Wave Equations in Geophysical Fluid Dynamics. Springer.

Durski, S.M., Glenn, S.M., Haidvogel, D.B., 2004. Vertical mixing schemes in the coastal ocean: comparison of the level 2.5 Mellor–Yamada scheme with an enhanced version of the K profile parameterization. J. Geophys. Res. 109, C01015.

Fringer, O.B., Armfield, S.W., Street, R.L., 2003. A nonstaggered curvilinear grid pressure correction method applied to interfacial waves. In: 2nd International Conference on Heat Transfer, Fluid Mechanics, and Thermodynamics (HEFAT), Victoria Falls, Zambia, Paper F01.

Garg, R.P., Ferziger, J.H., Monismith, S.G., 1997. Hybrid spectral finite difference simulations of stratified turbulent flows on distributed memory architectures. Int. J. Numer. Methods Fluids 24, 1129–1158.

Gargett, A.E., Wells, J.R., Tejada-Martnez, A.E., Grosch, C.E., 2004. Langmuir supercells: a mechanism for sediment resuspension and transport in shallow seas. Science 306, 1925–1928.

Gargett, A.E., Wells, J.R., 2007. Langmuir turbulence in shallow water: Part I. Observations. J. Fluid Mech. 576, 27–61.

Gargett, A.E., Savidge, D.K., 2008. The role of Langmuir supercells in seasonally tuned cross-shelf transport of bioactive material. Abstracts, AGU Ocean Sciences Meeting, Orlando, FL.

Germano, M., Piomelli, U., Moin, P., Cabot, W., 1991. A dynamic subgrid-scale eddy viscosity model. Phys. Fluids 3, 1760–1765.

Kim, J., Moin, P., Moser, R., 1987. Turbulence statistics in fully developed channel flow at low Reynolds number. J. Fluid Mech. 177, 133–166.

Kreiss, H.O., 1972. Difference approximations for boundary and eigenvalue problems for ordinary differential equations. Math. Comput. 26, 605–624.

Lamballais, E., Metais, O., Lesieur, M., 1998. Spectral-dynamic model for large-eddy simulations of turbulent rotating channel flow. Theor. Comput. Fluid Dyn. 12, 149–177.

Leibovich, S., 1983. The form and dynamics of Langmuir circulations. Annu. Rev. Fluid Mech. 15, 391–427.

Lele, S.K., 1992. Compact finite difference schemes with spectral-like resolution. J. Comput. Phys. 103, 16–42.

Lewis, D.M., Belcher, S.E., 2004. Time-dependent, coupled, Ekman boundary layer solutions incorporating Stokes drift. Dyn. Atmos. Oceans 37, 313–351.

Lewis, D.M., 2005. A simple model of plankton population dynamics coupled with a LES of the surface mixed layer. J. Theor. Biol. 223, 565–591.

Li, M., Sanford, L., Chao, S.-Y., 2005. Effects of time dependence in unstratified tidal boundary layers: results from large eddy simulations. Estuar. Coast. Shelf Sci. 62, 193–204.

Lilly, D.K., 1992. A proposed modification of the Germano subgrid-scale closure. Phys. Fluids 3, 2746–2757.

Lund, T.S., 1997. On the use of discrete filters for large-eddy simulation. In: Annual Research Briefs. Center for Turbulence Research, NASA Ames/Stanford University, pp. 83–95.

Lund, T., Poulos, G., Sullivan, P., 2003. LES of an Antarctic stable boundary layer using dynamic models. In: GEWEX Atmospheric Boundary Layer Study Workshop, Palma de Mallorca, Spain.

Mason, P.J., Thomson, D.J., 1992. Stochastic backscatter in large-eddy simulations of boundary layers. J. Fluid Mech. 242, 51–78.

McWilliams, J.C., Sullivan, P.P., Moeng, C.-H., 1997. Langmuir turbulence in the ocean. J. Fluid Mech. 334, 1–30.

Najjar, F.M., Tafti, D.K., 1996. Study of discrete test filters and finite difference approximations for the dynamic subgrid-scale stress model. Phys. Fluids 8, 1076–1088.

Piomelli, U., Balaras, E., 2002. Wall-layer models for large-eddy simulations. Annu. Rev. Fluid Mech. 34, 349–374.

Polton, J.A., Smith, J.A., MacKinnon, J.A., Tejada-Martnez, A.E., 2008. Rapid generation of high-frequency internal waves beneath a wind and wave forced oceanic surface mixed layer. Geophys. Res. Lett. 35, L13602.

Pope, S.B., 2000. Turbulent Flows. Cambridge University Press.

Porté-Agel, F., Meneveau, C., Parlange, M.B., 2000. A scale-dependent dynamic model for large-eddy simulation: application to a neutral atmospheric boundary layer. J. Fluid Mech. 415, 261–284.

Shih, T.M., Tan, C.H., Hwang, B.C., 1989. Effects of grid staggering on numerical schemes. Int. J. Numer. Methods Fluids 9, 193–212.

Skyllingstad, E.D., Denbo, D.W., 1995. An ocean large-eddy simulation of Langmuir circulations and convection in the surface mixed layer. J. Geophys. Res. 100, 8501–8522.

Slinn, D.N., Riley, J.J., 1998. A model for the simulation of turbulent boundary layers in an incompressible stratified flow. J. Comput. Phys. 144, 550–602.

Smagorinsky, J., 1963. General circulation experiments with the primitive equations. I. The basic experiment. Mon. Weather Rev. 91, 99–164.

Sullivan, P.P., McWilliams, J.C., Moeng, C.-H., 1994. A subgrid-scale model for large-eddy simulation of planetary boundary-layer flows. Bound. Layer Meteor. 71, 247–276.

Tejada-Martínez, A.E., Grosch, C.E., 2007. Langmuir turbulence in shallow water: Part II. Large-eddy simulation. J. Fluid Mech. 576, 63–108.

Tejada-Martínez, A.E., Grosch, C.E., Gatski, T.B., 2007. Temporal large-eddy simulation of unstratified and stratified turbulent channel flows. Int. J. Heat Fluid Flow 28, 1244–1261.

Tsukahara, T., Kawamura, H., Shinghai, K., 2006. DNS of turbulent Couette flow with emphasis on the large-scale structure in the core region. J. Turbul. 7, 19.

Winters, K.B., MacKinnon, J.A., Mills, B., 2004. A spectral model for process studies of rotating density-stratified flows. J. Atmos. Ocean. Technol. 21, 69–94.

Zikanov, O., Slinn, D.N., Dhanak, M.R., 2003. Large-eddy simulations of the wind-induced turbulent Ekman layer. J. Fluid Mech. 495, 343–368.